

The Hawaiian SWELL Pilot Experiment - Evidence for Lithosphere Rejuvenation from Ocean Bottom Surface Wave Data

G. Laske¹, J. Phipps Morgan² and J. A. Orcutt¹

¹*Cecil H. and Ida M. Green Institute of Geophysics and Planetary Physics, Scripps Institution of Oceanography,
University of California San Diego, 9500 Gilman Drive, La Jolla, CA 92093-0225, USA.*

²*Department of Earth & Atmospheric Sciences, Snee Hall, Cornell University, Ithaca, New York, NY14853-1504*

1 ABSTRACT

During the roughly year-long SWELL pilot experiment in 1997/1998, eight ocean bottom instruments deployed to the southwest of the Hawaiian Islands recorded teleseismic Rayleigh waves with periods between 15 and 70 s. Such data are capable of resolving structural variations within the oceanic lithosphere and upper asthenosphere and therefore help understand the mechanism that supports the Hawaiian Swell relief. The pilot experiment was a technical as well as a scientific feasibility study and consisted of a hexagonal array of Scripps "L-CHEAPO" instruments using differential pressure sensors. The analysis of 84 earthquakes provided numerous high-precision phase velocity curves in an unprecedented wide period range. We find a rather uniform (unaltered) lid at the top of the lithosphere that is underlain by a strongly heterogeneous lower lithosphere and upper asthenosphere. Strong slow anomalies appear within roughly 300 km of the island chain and indicate that the lithosphere has been altered most likely by the same process that causes the Hawaiian volcanism. The anomalies increase with depth and reach well into the asthenosphere suggesting a sub-lithospheric dynamic source for the swell relief. The imaged velocity variations are consistent with thermal rejuvenation but our array did not appear to have covered the melt generating region of the Hawaiian hotspot.

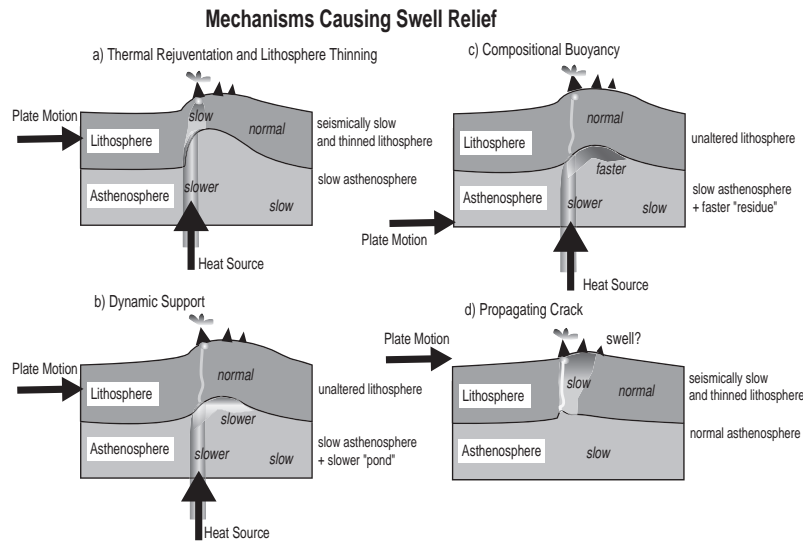


Fig. 1. Concept figure for four possible mechanisms for hot spot swells. Thermal rejuvenation and the propagating crack model predict a significant impact on the lithosphere but the latter is associated with normal asthenosphere. The dynamic support and the compositional buoyancy model have an unaltered lithosphere but an anomalous asthenosphere.

2 INTRODUCTION

The Hawaiian hot spot and its island chain are thought to be the textbook example of a hot spot located over a deep-rooted mantle plume (Wilson, 1963; Morgan, 1971). Since plume material is expected to ascend in a much more viscous surrounding mantle, it is expected to stagnate near the top and exhibit a sizable plume head that eventually leads to the uplift of the overlying seafloor (e.g. Olson, 1990). A hot spot on a stationary plate may then develop a dome-shaped swell (e.g. Cape Verde) while a plate moving above a plume would shear it and drag some of its material downstream, creating an elongated swell (Olson, 1990; Sleep, 1990). Hawaii's isolated location within a plate, away from plate boundaries should give scientists the opportunity to test most basic hypotheses on plume-plate interaction and related volcanism. Yet, the lack of many crucial geophysical data has recently revived the discussions on whether even the Hawaiian hot spot volcanism is related to a deep-seated mantle plume or is rather an expression of propagating cracks in the lithosphere (Natland and Winterer, 2005). Similarly, the dominant cause of the Hawaiian Swell relief has not yet been conclusively determined. At least three mechanisms have been proposed (Figure 1 see e.g. Phipps Morgan et al., 1995) – a) thermal rejuvenation; b) dynamic support; c) compositional buoyancy – but none of them is universally accepted as a single dominant mechanism. All these mechanisms create a buoyant lithosphere, and so can explain the bathymetric anomalies, but they have distinct geophysical responses and each model currently appears to be inconsistent with at least one observable.

2.1 Possible Causes for Swell Relief

In the *thermal rejuvenation model* the lithosphere reheats and thins when a plate moves over a hotspot (Figure 1). It explains the uplift of the seafloor and the age-dependent subsidence of seamounts along the Hawaiian island chain (Crough, 1978; Detrick and Crough, 1978). This model was reported to be consistent with gravity and geoid anomalies and observations suggest a compensation depth of only 40–90 km (instead of the 120 km for 90 Ma old lithosphere). Initially, rapid heating within 5 Ma of the lower lithosphere (40–50 km) and subsequent cooling appeared broadly consistent with heat flow data along the swell (von Herzen et al., 1982) though Detrick and Crough (1978) had recognized that the reheating model does not offer a mechanism for the rapid heating. The heatflow argument was later revised when no significant anomaly was found across the swell southeast of Midway (von Herzen et al., 1989) though the interpretation of those data is still subject of debate (McNutt, personal communication). The thermal rejuvenation model has received extensive criticism from geodynamicists as it is unable to explain the rapid initial heat loss by conduction alone and modeling attempts fail to erode the lithosphere significantly if heating were the only mechanism involved (e.g. Ribe and Christensen, 1994; Moore et al., 1998). The *dynamic support model* is a result of early efforts to reconcile gravity and bathymetry observations of the Hawaiian Swell (Watts, 1976). Ponding, or pancaking, of ascending hot asthenosphere causes an unaltered lithosphere to rise. A moving Pacific plate shears the ponding mantle material and drags it along the island chain, thereby causing the elongated Hawaiian Swell (Olson, 1990; Sleep, 1990). The compensation depth for this model remains at 120 km depth. An unaltered lithosphere is, however, inconsistent with the heatflow data along the swell (von Herzen et al., 1989) and the geoid. A recent hybrid model – dynamic thinning – in which secondary convection in the ponding asthenosphere erodes the lithosphere downstream (Ribe, 2004) appears to find support by a recent seismic study (Li et al., 2004). The third model, *compositional buoyancy*, was suggested by Jordan (1979) and is based on the idea that the extraction of melt by basaltic volcanism leaves behind a buoyant, low-density mantle residue (see also Robinson, 1988). Of the models describe here, this is the only one that predicts high seismic velocities in the lithosphere. At this point, it is unclear if propagating cracks in the lithosphere could produce enough buoyant material for a swell (Jerry Winterer, personal communication). A cracking lithosphere would most likely have the seismic signature of some degree of rejuvenation but the asthenosphere below should be normal.

2.2 The Hawaiian Hot Spot and Seismic Tomography

Seismology provides useful tools to identify and image the seismic imprint of a mantle plume or other source for hot spot volcanism. Assuming thermal derivatives, $\partial v/\partial T$, near $1 \times 10^{-4} \text{K}^{-1}$ (Karato, 1993), thermal

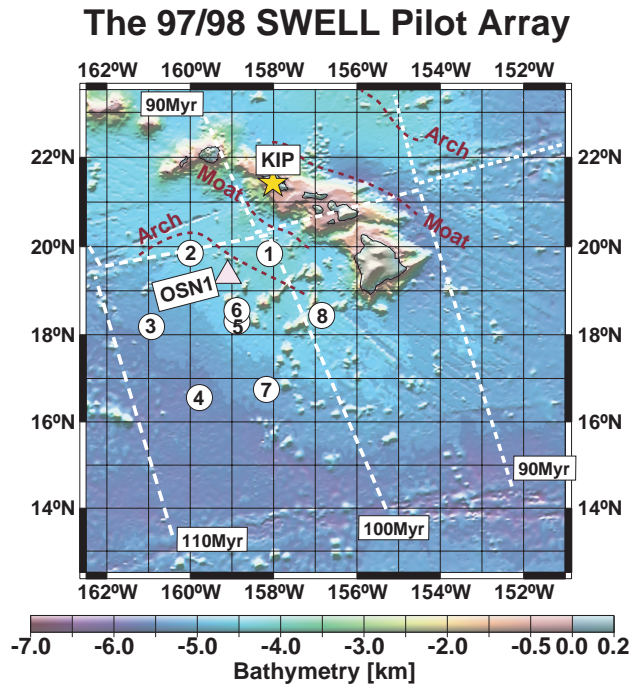


Fig. 2. Location map of the SWELL pilot experiment which collected data continuously from April 1997 through May 1998. The array covered the southwestern margin of the Hawaiian Swell which is characterized by its shallow bathymetry. Also marked are the ocean seismic network pilot borehole OSN1 (February through June 1998) and permanent broad-band station KIP (Kipapa) of the global seismic network (GSN) and GEOSCOPE. Dashed lines mark the age of the ocean floor (Müller et al., 1997).

plumes with excess temperatures of a few 100 K give rise to changes of upper mantle seismic velocities by a few per cent, which should be resolvable by modern seismic tomography. Nevertheless, progress has been slow, especially in the imaging of a Hawaiian plume. Global body wave tomographic models often display a low-velocity anomaly near Hawaii in the upper mantle (e.g. Grand et al., 1997) and a recent study cataloged the seismic signature of plumes (Montelli et al., 2006) to reassess heat and mass fluxes through plumes (Nolet et al., 2006). However, such models typically have poor depth resolution in the upper few 100 km unless the dataset contains shallow–turning phases or surface waves (which both cited studies do not have). Further complicating imaging capabilities with global data is the fact that the width of the plume conduit is expected to be of the order of only a few 100 km. Such a small structure is near the limits of data coverage, the model parameterization and the wavelength of the probing seismic waves and proper imaging may require the use of a finite–frequency approach (Montelli et al., 2006). Surface waves should be capable to sense a shallow wide plume head but global dispersion maps at 60s, with signal wavelengths of 250 km, largely disagree on even the approximate location of a possible low–velocity anomaly near Hawaii (e.g. Laske and Masters, 1996;

Trampert and Woodhouse, 1996; Ekström et al., 1997; Ritzwoller et al., 2004; Maggi et al. 2006). The reason for this is that the lateral resolution of structure around Hawaii is rather poor, due to the lack of permanent broadband seismic stations.

Regional body wave tomography using temporary deployments of broadband arrays have come a long way to image plume-like features on land (e.g. Wolfe et al, 1997; Keyser et al., 2002; Schutt and Humphreys, 2004) but similar studies at Hawaii are extremely limited, due to the nearly linear alignment of the islands (e.g. Wolfe et al, 2002). Such studies usually also do not have the resolution within the lithosphere and shallow asthenosphere to distinguish between the three models proposed for the swell uplift, but surface waves studies do. The reheating model causes low seismic velocities in the lower lithosphere, while normal velocities would be found for the dynamical support model (Figure 1). The compositional buoyancy model predicts high velocities which are claimed to have been found by Katzman et al. (1998) near the end of a corridor between Fiji/Tonga and Hawaii. Surface wave studies along the Hawaiian Islands have found no evidence for lithospheric thinning (Woods et al., 1991; Woods and Okal, 1996; Priestley and Tilmann, 1999) though shear velocities in the lithosphere appear to be at least 2.5% lower between Oahu and Hawaii than downstream between Oahu and Midway. These studies used the two-station dispersion measurement technique between only one station pair. It has been argued that the resulting dispersion curves in this case may be biased high because laterally trapped waves along the swell may not have been accounted for properly (Maupin, 1992). What is obviously needed are constraints from crossing ray paths that can be obtained only from broadband observations on ocean bottom instruments deployed around the Hawaiian Swell.

Prior to the MELT (Mantle Electromagnetic and Tomography) experiment (Forsyth et al., 1998) across the relatively shallow East Pacific Rise, extensive long-term deployments were not possible due to the prohibitively high power demand of broadband seismic equipment. In 1997, we received NSF funding to conduct a year-long proof-of-concept deployment for our proposed SWELL Experiment (Seismic Wave Exploration in the Lower Lithosphere) near Hawaii (Figure 2). Eight of our L-CHEAPO (Low-Cost Hardware for Earth Applications and Physical Oceanography) instruments (Willoughby et al., 1993) were placed in a hexagonal array across the southwestern margin of the Hawaiian Swell to record Rayleigh waves at periods beyond the microseism band (15 s and longer). Unlike in the MELT experiment that used a combination of three-component seismometers and pressure sensors, the sole sensor used in our deployment was a broadband Cox-Webb pressure variometer that is commonly known as a differential pressure gauge (DPG) (Cox et al., 1984). The use of such sensors was met with some skepticism and the interested reader is referred to GSA data repository electronic supplement ###, Appendix B. The proximity to the OSN borehole seismometer test site at ODP borehole 843B south of Oahu allowed us to compare our data with observatory quality broadband seismometer data collected by much more expensive seafloor equipment (Vernon et al., 1998). To support or

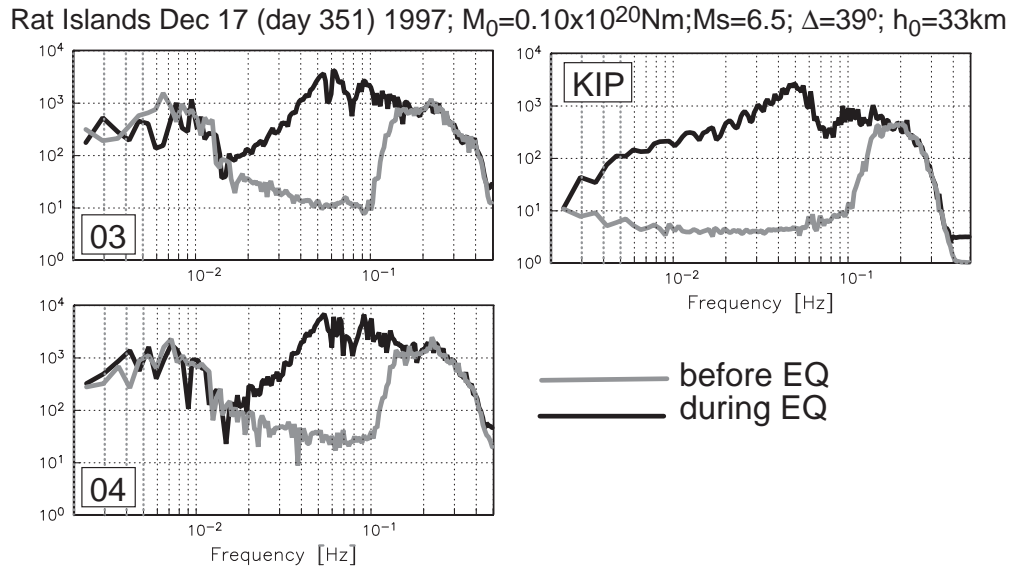


Fig. 3. Ambient noise and earthquake amplitude spectra for the Rat Island event shown in Laske et al. (1999), at sites #3 and #4. Also shown are the spectra for the very-broadband Wielandt–Streckeisen STS–1 vault seismometer at the permanent station KIP, the global seismic installation with possibly the lowest long-period vertical-component noise levels. Spectra are calculated using 28-min long boxcar windows before and during the event. The instrument response is not removed to avoid possible numerical contamination near the roll-off ends of the responses.

refute the dynamic support model for the Hawaiian Swell, structure has to be recovered reliably down to at least 130 km. It is therefore essential to measure dispersion successfully down to at least 20 mHz (see GSA data repository electronic supplement ###, Appendix B for details). GSA data repository electronic supplement ###, Appendix A describes the field program. It turns out that the collected dataset is of an unprecedented bandwidth, quality and richness in signal that has gone beyond our expectations to retrieve the average structure beneath the pilot array (Laske et al., 1999). In the following, we present data examples, dispersion curves along two-station legs and a 3D-model across the margin of the Hawaiian Swell. The model is non-unique and we discuss possible aspects that can influence the retrieval of a model. Finally, we discuss the consistency of our model with several other geophysical observables.

3 DATA EXAMPLES

3.1 Spectra to Assess Signal-to-Noise Characteristics

During the deployment from April 1997 through May 1998, we recorded 84 shallow teleseismic events at excellent signal-to-noise levels. The azimuthal data coverage is as good as any 1-year long deployment can achieve (Laske et al., 1999). For many of these events, we are able to measure the dispersion at periods

Off Southern Chile, Apr 01, 98; 22:43:00 UTC;
 $h_0=9\text{km}$; $\Delta=97^\circ$; $M_s=6.0$; $M_0=0.12 \times 10^{20}\text{Nm}$

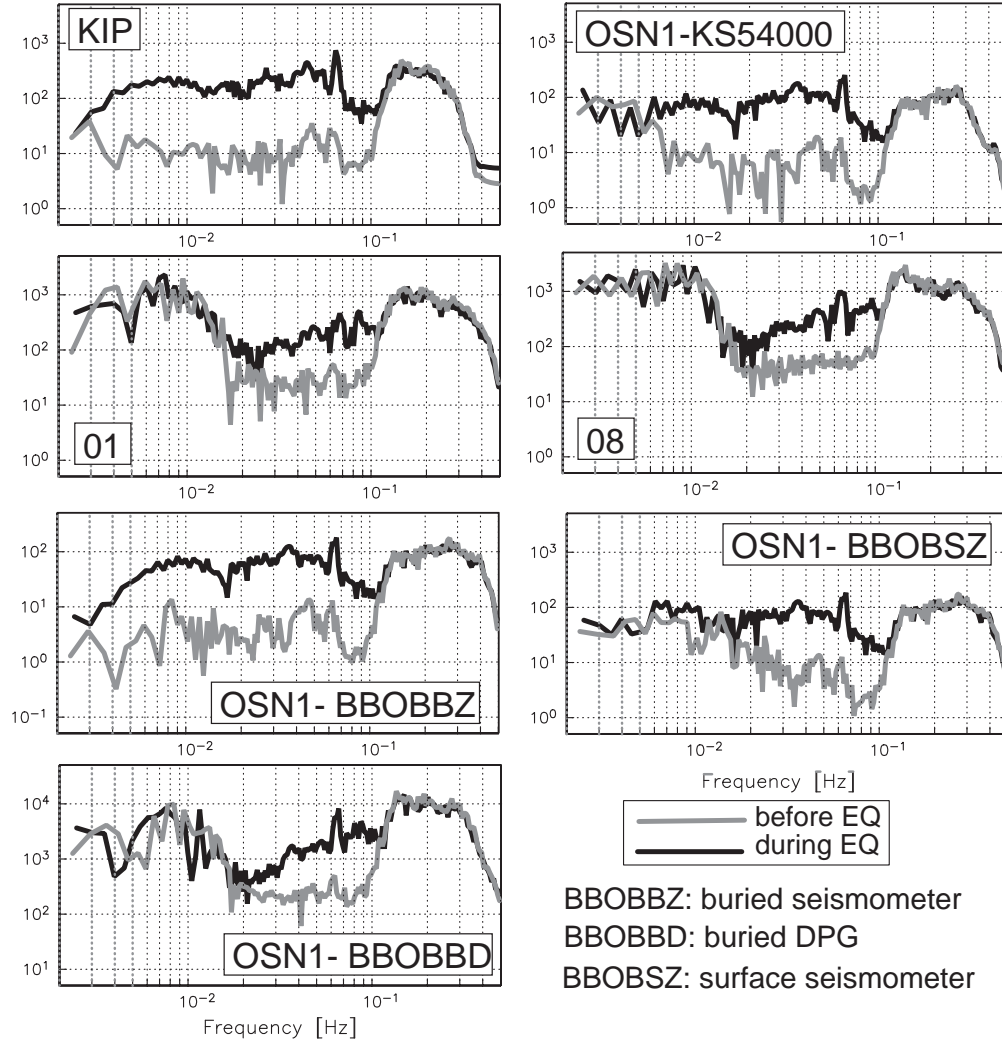


Fig. 4. Noise and signal amplitude spectra calculated for an earthquake off the coast of Southern Chile, at sites #1 and #8. Also shown are spectra at land-station KIP, from the very-broadband borehole sensor (KS54000) at OSN1, and from OSN1 broadband buried and surface instruments. BBOBS stands for "broadband ocean bottom seismometer". For details see Figure 3.

between 17 and 60 s, sometimes even beyond 70 s. Figure 3 shows an example of ambient noise and earthquake spectra. On the high-frequency end the SWELL stations exhibit pronounced microseism peaks centered at about 0.2 Hz. Equally large is the noise at infragravity frequencies below 0.015 Hz (see also Webb, 1998) which limits our ability to measure dispersion at very long periods. Nevertheless, the earthquake signal stands out clearly above the noise floor at frequencies below 0.15 Hz. Signal can be observed down to at least

0.015 Hz (at site #3) which may not have been achieved on previous OBS deployments. Comparing the spectra with those at station KIP it is quite clear that the earthquake generated observable signal at frequencies below 0.01 Hz but the noisy environment on the ocean floor did not allow us to observe this. It is somewhat curious but not well understood that the long-period noise floor at KIP is one of the lowest if not the lowest of all GSN stations.

Figure 4 compares our spectra with others collected during the OSN1 pilot deployment. As for the Rat Island event, the spectra at KIP show that the event generated observable signal far below 0.01 Hz. The signal-to-noise ratio is not as good as that of the Rat Island event which was closer to the stations and whose surface wave magnitude was larger. Nevertheless, we are able to observe signal on the SWELL instruments to frequencies below 0.02 Hz. Also shown are the spectra at the very-broadband Teledyne-Geotech KS54000 borehole seismometer at OSN1. The KS54000 is often used at GSN stations as alternative to the STS-1. At this instrument, the noise floor grows above the signal level at about 0.006 Hz and one could be misled to believe that this is infragravity noise. A broadband Güralp CMG-3T seismometer that was buried just below the seafloor (Collins et al., 1991) appears much quieter. The KS54000 was deployed at 242 m depth below the seafloor in a borehole that reached through 243 m of sediments and 70 m into the crystalline basement (Dziewonski et al., 1991; Collins et al., 1991). During a test-deployment of this sensor at our test facility at Piñon Flat (PFO), the seismometer had problems with long-period noise and it was conjectured that water circulating in the borehole caused the noise (Frank Vernon, personal communication). It is obviously possible to achieve an impressive signal-to-noise ratio with buried OBS equipment but such deployment methods are probably prohibitively costly for large-scale experiments. A CMG-3T deployed on the seafloor exhibits high noise levels in the infragravity band and probably does not allow us to analyze long-period signal beyond of what is achieved on the SWELL DPG. Note that the pressure signal from the earthquake is quite different from the ground motion signal but the crossover of noise and earthquake signals occur at similar frequencies though the overall signal-to-noise ratio appears to be slightly better in ground motion. Also shown are the spectra of the buried DPG which are virtually identical to the unburied ones. Burying a pressure sensor therefore does not appear to have any benefits. Regarding the seismic bandwidth, our data are favorably compatible with that of the MELT experiment (Forsyth et al., 1998).

3.2 Time Series to Assess Signal Coherence

Figure 5 shows the record sections for two earthquakes off the Coast of Chile that were about 1000 km apart. Except for the record at site #5 for the April 98 event of Figure 4, The SWELL records compare well with those at stations KIP and OSN1. We notice that some of the energy at periods shorter than 25 s appears to

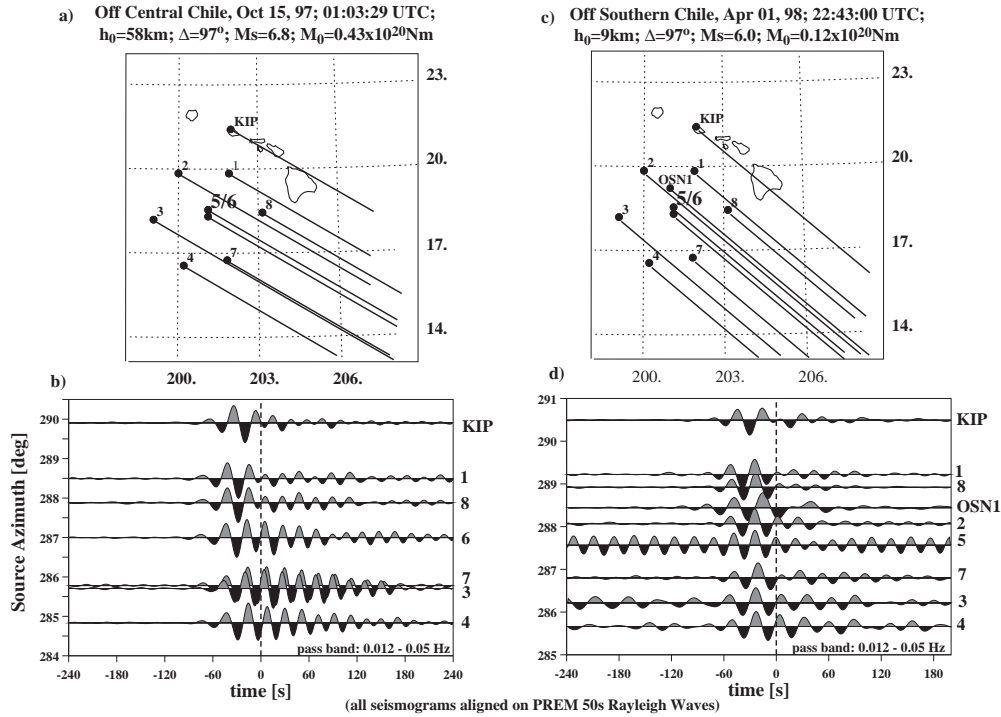


Fig. 5. Record sections of two earthquakes off the coast of Chile. Records are shown for our SWELL sites as well as of the observatory quality stations KIP and OSN1. The records are aligned relative to PREM 50s Rayleigh wave arrival times (Dziewonski and Anderson, 1981). They are band-pass filtered using a zero-phase shift 5-step Butterworth filter in the frequency band indicated above the section. Records are not corrected for instrumental effects, i.e. phase shifts between KIP and DPGs may not be due to structure. Differences in the waveforms at sites #1, #8 and KIP are most likely due to structural variations near Hawaii. The record of OSN1 for the April 98 event is shifted upward for better comparison.

be diminished at stations KIP, #1 and #8, implying a local increase in attenuation or diffraction though some of this may also be explained by source radiation. Figure 6 shows examples for three events in Guatemala. Great waveform coherency is apparent, even for smaller events. The overall good signal-to-noise conditions in our deployment allows us to analyze events with surface wave magnitudes down to $M_S = 5.5$.

We notice some noise contamination, e.g. at station #5 for the December 97 Guatemala and April 98 Chile events, and #3 for the March 98 event. The noise is extremely intermittent, typically lasting for a few hours, and is confined to a narrow band at about 30 s (though this varies with time) and has one or two higher harmonics. The noise does not compromise data collection severely but some individual phase measurements have to be discarded as we do not attempt to correct for the noise. This problem has not been noticed before as we were the first group to use this equipment for observing long-period signals. After carefully analyzing

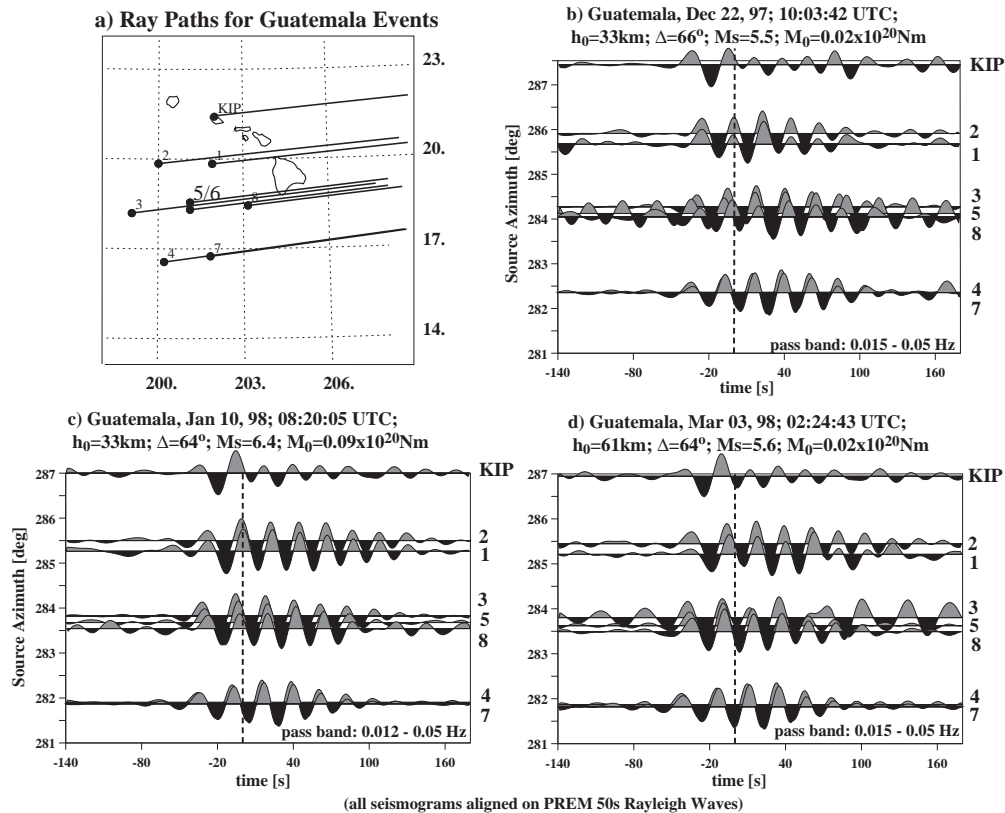


Fig. 6. Record sections of three earthquakes in Guatemala. The epicentral distance was about 65° for all events. The December 97 and the March 98 events were more than four times smaller than the January 98 event. Noise observed for these are transient, nearly harmonic and affect individual instruments only and not the whole array. For details see Figure 5.

the nature of the noise we conclude that its origin is most likely not environmental but instrumental and due to two beating clocks on the datalogger and the sensor driver boards.

Figure 6 suggests that subtle relative waveform delays are repeatable. The traces of stations #1,2 and #8 are delayed, though the delay at #2 is small, and those of #4 and #7 are clearly advanced. The delay between #1/#8 and #4/#7 amounts to 5.7 s. In principle, the delay can have been accumulated anywhere between Guatemala and the array but if the slow structure was far from Hawaii, the record at #3 should also be delayed. A similar delay can be found for events from Venezuela, Colombia and other events in the northern quadrant. We do not observe this delay for earthquakes whose rays do not cross the islands before arriving at the array (i.e. the events in Chile, Tonga, Fiji and along the Western Pacific Ocean). Taking into account the reduced amplitudes at #1 and #8 for the Chile events, we infer a strong anomaly near the islands, with a maximum extent possibly beyond sites #1 and #8, but likely diminished. Since #4 and #7 are not affected, the delay may obviously be associated with a thickened crust beneath the Hawaiian ridge (see GSA

data repository electronic supplement ###, Appendix C). The dominant period in the seismograms is about 22 s. At a phase velocity of roughly 4 km/s, the observed delay amounts to a phase velocity anomaly of at least 6.5%. A thickened crust can explain only about 2% but not much more. Rayleigh waves at these periods are sensitive to upper mantle structure down to at least 60 km and we gather first evidence that a low-velocity body in the mantle causes our observations.

4 PHASE MEASUREMENTS ACROSS THE PILOT ARRAY

Our phase velocity analysis involves 3 steps: a) measure frequency-dependent phase, b) determine phase velocity curves, c) invert phase velocity curves for structure at depth. For each event, we measure the frequency-dependent phase at one station with respect to those of all the others, using the transfer function technique of Laske and Masters (1996). A multi-taper approach improves bias conditions in the presence of noise and provides statistical measurement errors. From the phase data, we then determine phase velocities. We seek to apply methods that do not require the knowledge of structure between earthquake sources and our array. For example, incoming wavefronts can be fit to all phases measured in a station subarray to determine average velocities within this array (e.g. Stange and Friederich, 1993; Laske et al., 1999). A multi-parameter fit allows the wavefronts to have simple or complex shapes and oblique arrival angles (Alsina and Snieder, 1993). The latter accounts for the fact that lateral heterogeneity between source and the array refracts waves away from the source-receiver great circles. Fitting spherical instead of plane waves significantly improves the fit to our data and provides more consistent off-great circle arrival angles but more complicated wavefronts are not necessary for circum-Pacific events. Events occurring in the North Atlantic, Indian Ocean or Eurasia exhibit highly complex waveforms that are sometimes not coherent across the array. Such events are associated with waves traveling across large continental areas and most likely require the fitting of complex wavefronts, a process which is highly non-unique (e.g. Friederich et al., 1994). We therefore discard such events. We are left with 58 mainly circum-Pacific events for which stable phase velocity estimates are possible. We will use the triangle technique in a later section to validate the 2D-phase velocity variations resulting from a comprehensive two-station approach.

The two-station approach lets us best assess lateral variations across the array without having to resort to modeling structure outside the pilot array. This requires earthquakes that share the same great circle as a chosen two-station leg. Since this is almost never achieved, we have to choose a maximum off-great circle tolerance which is done individually for each station leg. Station #2 was operating only during the second deployment so the maximum allowed angle of 20° is relatively high. The tolerance for other legs can be as low as 8° and still provide as many as 8 earthquakes. An off-great circle approach of 20° effectively shortens

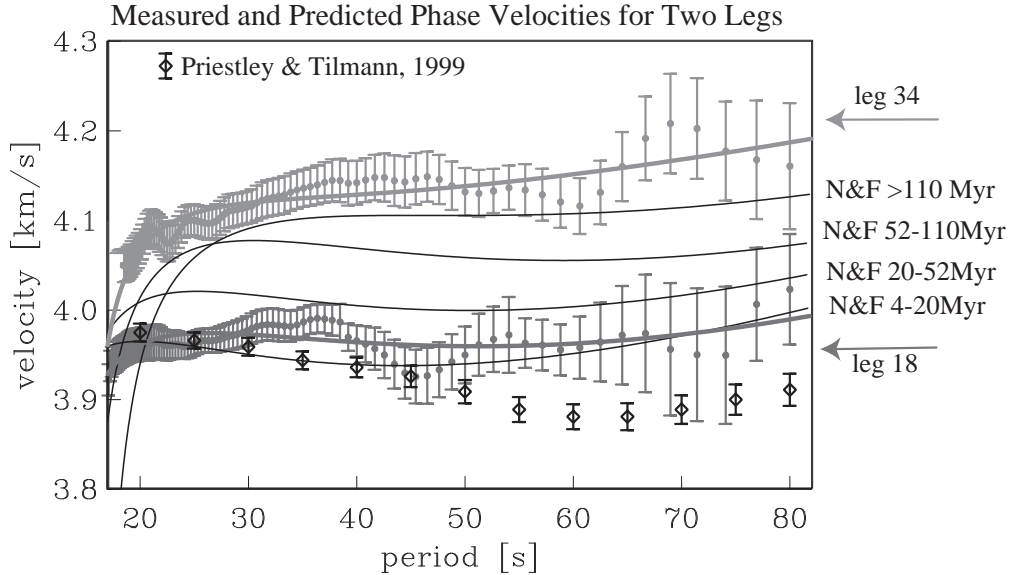


Fig. 7. Path-averaged phase velocity along the 2 parallel station legs 1–8 and 3–4, together with the curves calculated for the best-fitting models obtained in our inversions (Figures 10 and 11). The error bars reflect 1σ variations of several dispersion curves obtained for the same 2-station leg. Also shown are the age-dependent phase velocities by Nishimura and Forsyth (1989) (N&F) and observed phase velocities by Priestley and Tilmann (1999) between the islands of Oahu and Hawaii.

the actual travel path by 6%. We correct for this to avoid phase velocity estimates to be biased high. We also have to take into account off-great circle propagation due to lateral refraction. With the spherical wave fitting technique, we rarely find approaches away from the great-circle direction by more than 5° . The average is 2.6° which accounts for a 0.1% bias. This is within our measurement uncertainties and we therefore do not apply additional corrections. Events with larger arrival angles, such as the great March 25, 1998 Balleny Island event are typically associated with complicated waveforms due either to the source process, relative position of the array to the radiation pattern or propagation effects. We therefore exclude such events (a total of 8) from the analysis.

5 LATERAL VARIATIONS ACROSS THE SWELL PILOT ARRAY

Figure 7 shows path-averaged dispersion curves for two nearly parallel 2-station legs. Both legs are roughly aligned with the Hawaiian Ridge but while leg 1–8 is on the swell, leg 3–4 is in the deep ocean and is thought to traverse unaltered ca. 110 Ma old lithosphere. The dispersion curve for leg 1–8 is based on data from 8 events (Aleutian Islands, Kamchatka, Kuril Islands and Chile), while that for 3–4 is based on 6 events. The two curves are significantly different, with the leg 1–8 curve being nearly aligned with the Nishimura and

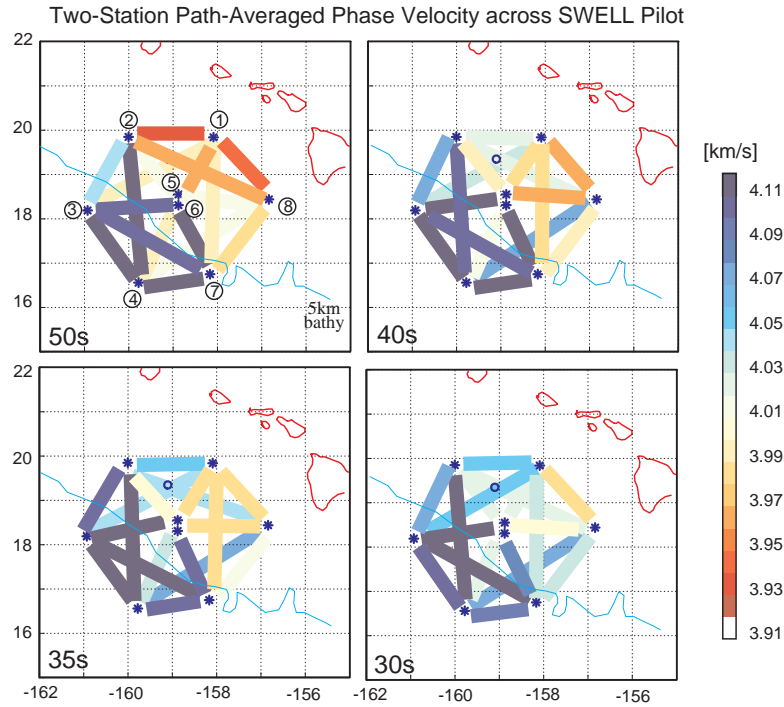


Fig. 8. Path-averaged phase velocities across the SWELL pilot array, as function of period. The most prominent feature is a strong velocity gradient across the SWELL margin, with lower velocities found near the islands.

Forsyth (1989) (N&F) prediction for extremely young lithosphere, while the leg 3–4 curve is slightly above the N&F curve for lithosphere older than 110 Ma. Also shown is the dispersion curve obtained by Priestley and Tilmann (1999) (P&T) between the islands of Oahu and Hawaii along the Hawaiian Ridge. Their curve is slightly lower than our 1–8 curve and lies just outside our measurement errors. The fact that the P&T curve is lower than the 1–8 curve is expected since the largest mantle anomalies associated with plume–lithosphere interaction should be found along the Hawaiian Ridge. With about 5% at 40s, the difference in dispersion between legs 3–4 and 1–8 is remarkable considering that the associated structural changes occur over only 350 km, but it is not unrealistic. We are somewhat cautious to interpret isolated two–station dispersion curves since lateral heterogeneity away from the two–station path and azimuthal anisotropy along the path have an impact on path–averaged two–station dispersion. The analysis of crossing paths in Figure 8 helps diminish this deficiency. Perhaps an indication that the bias cannot be severe is the fact that other parallel two–station legs that have entirely different azimuths exhibit similar heterogeneity (e.g. legs 2–1 and 4–7). Results from crossing two–station legs scatter somewhat but are marginally consistent. The most obvious and dominant feature is a pronounced velocities gradient from the deep ocean toward the islands. This gradient can be observed at all periods but is strongest at longer periods.

In principle, the observation of lower velocities near the islands would be consistent with changes in crustal structure but a thickened oceanic crust could account for no more than 1.5%. There is no evidence that the crust changes dramatically across the array (see GSA data repository electronic supplement ###, Appendix C). A change in water depth across the array has some impact, but only at periods shorter than 30 s. The influence of water depth can be ruled out here because the effect has the opposite sign, i.e. a *decreasing* water depth *increases* velocities. Since longer periods are affected more than short periods, anomalies at depth must be distributed either throughout the lithosphere or a pronounced anomaly is located in the lower lithosphere or deeper. Rayleigh waves at 50 s are most sensitive to shear velocity near 80 km depth but the anomaly could reach as deep as 150 km, or deeper (Figure 20 in GSA data repository electronic supplement ###, Appendix B). A marked increase in measurement errors beyond about 67 s/ 15 mHz is associated with the fact that dispersion measurements become uncertain when the signal wavelength approaches the station spacing. We therefore expect a degradation of resolution at depths below 150 km.

6 INVERSION FOR STRUCTURE AT DEPTH

In order to retrieve structure at depth, we perform two-step inversions. First we determine path-averaged depth-profiles along each two-station leg. All profiles are then combined in an inversion for 3D structure.

Surface waves are sensitive to V_S , V_P and density, ρ but the most dominant and best resolved parameter is V_S (GSA data repository electronic supplement ###, Appendix B). In order to limit the number of model parameters for a well conditioned inverse problem, tomographers often ignore sensitivity to V_P and ρ . Such a strategy could lead to biased models where shallow V_P structure can be mapped into deeper V_S structure. We prefer to scale the kernels for V_P and ρ and include them in a single kernel for V_S , using the following scaling:

$$\begin{aligned} \tilde{A} \cdot \delta\alpha &= (1/1.7)\tilde{B} \cdot \delta\beta \\ \tilde{R} \cdot \delta\rho &= (1/2.5)\tilde{B} \cdot \delta\beta \end{aligned} \tag{1}$$

The scaling factors have been determined in both theoretical and experimental studies (e.g. Anderson et al., 1968; Anderson and Isaak, 1995), for high temperatures and low pressures such as we find in the upper mantle. They are applicable as long as strong compositional changes or large amounts of melt (i.e. > 10%) do not play a significant role. We use a modified N&F model for 52–110 Ma old lithosphere as starting model. It is parameterized in 17 constant layers whose thickness is 7 km near the top but then increases with depth to account for the degrading resolution. Since the 90 s data are sensitive to structure beyond 200 km, our bottom layer is 50 km thick and ends at 245 km. Velocities retrieved at these depths are extremely uncertain and are excluded from later interpretation but including such a layer in the inversion avoids artificial mapping of

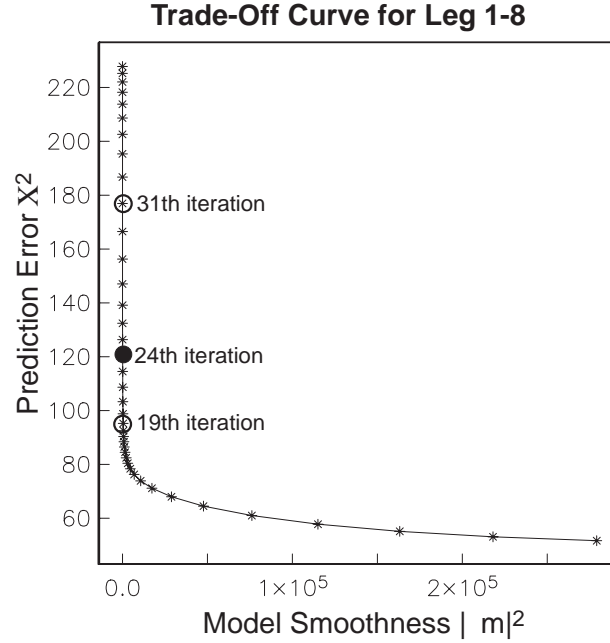


Fig. 9. Trade-off curve for station leg 1–8. Displayed is the data prediction error and model smoothness as function of the regularization parameter, μ . The location of the final model (24th iteration) is marked as well as the range of acceptable models that lie within the "model error range" of Figure 10. The chosen models have misfits, χ^2/N , between 1.0 and 1.9.

deep structure into shallower layers. The crust is adjusted using the model described in GSA data repository electronic supplement ###, Appendix C. We also adjust for two–station path–averaged water depths.

We seek smooth variations to the starting model that fit our data to within an acceptable misfit, χ^2/N , where $\chi = x_d - x_t$, x_d is the datum, x_t the prediction and N the number of data. Formally, we seek to minimize the weighted sum of data prediction error, χ^2 , and model smoothness, $\partial \mathbf{m}$

$$\chi^2 + \mu \left| \mathbf{m}^T \partial^T \partial \mathbf{m} \right| \tag{2}$$

where \mathbf{m} is the model vector and μ the smoothing or regularization parameter. The trade-off between the two terms is shown in (Figure 9). The shape of the trade-off curve depends on the data errors as well as the composition of the dataset but the resulting optimal model is actually similar to the one shown here. In practice, models that are very close to the minimum of equation 2 are highly oscillatory and we choose smoother models. Model errors can be obtained from the data errors through a formal singular value decomposition or by Monte Carlo forward modeling. Here we show the range of acceptable models along the tradeoff curve. The final model has a mistfit, χ^2/N , of 1.3 so is slightly inconsistent with the data.

The final model in Figure 10 is significantly slower than the N&F model for 52-110 Ma old lithosphere

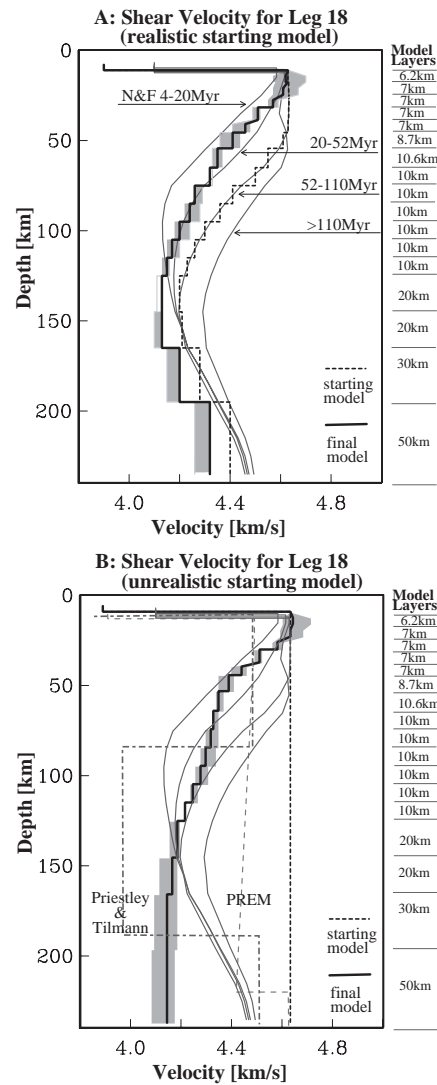


Fig. 10. Shear velocity models for the two-station leg 1–8. A: Model obtained using the modified Nishimura and Forsyth 52-110Myr starting model. The predictions for this model are shown in Figure 7. The grey area marks the range of models along the trade-off curve that still fit the data to a given misfit (see Figure 9).

B: Model obtained using a constant velocity as starting model. In the upper 75 km, the final model is very similar to the model in A but is faster down to 150 km and the significantly slower. Also shown are model PREM, the age-dependent models by Nishimura and Forsyth (1989) and the model by Priestley and Tilmann (1999) between the islands of Oahu and Hawaii.

below about 30 km. Our model follows that of the N&F model for 20-52 Ma old lithosphere down to about 120 km below which depth it remains somewhat slower. While the velocities are relatively poorly constrained at depths below 170 km, the difference to the N&F model at shallower depths is significant and indicates that the cooling lithosphere has been altered at its base through secondary processes. Models derived from surface

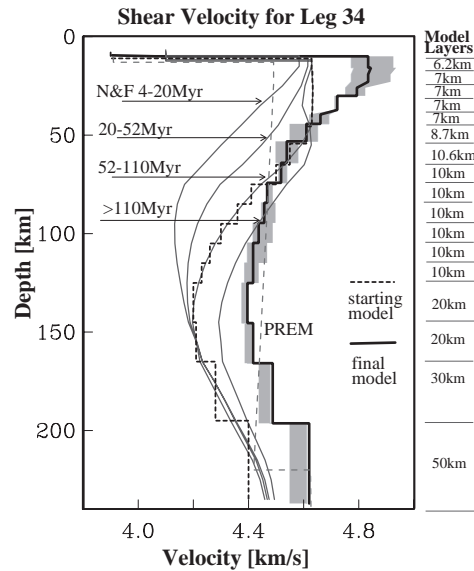


Fig. 11. Shear velocity model for the two–station leg 3–4. For details see Figure 10.

waves are non–unique. If we had chosen less layers, such as the two–layer parameterization of Priestley and Tilmann (1999), the resulting velocity above 80 km may be similar to their velocity which is close to the velocity of PREM (Dziewonski and Anderson, 1981). Below 80 km, our model is significantly faster than the P&T model which is in agreement with the fact that our dispersion curve is systematically faster than theirs. Inversions can get caught in a local minimum and the model presented here may not be the actual solution to minimizing equation 2. In Figure 10b, we show the final model for a different starting model which is rather unrealistic but helps illuminate how the final model depends on the starting model. This model (model B) is virtually identical to our preferred model (model A) down to 70 km but then oscillates more significantly around the N&F model for 20–52 Ma. Higher velocities are found down to about 150 km while much lower velocities are found below that, though they remain above the Priestley and Tilmann (1999) velocities. The misfit of this model is slightly less than that of model A ($\chi^2 = 1.19$) but we nevertheless discard it as an improbable solution. In a hypothesis test, we remove one deep layer after the other and test the misfit. We would expect that the misfit does not decrease dramatically initially, due to the decreased sensitivity at great depth. This is the case for model A where the misfit increases by 1.6% when omitting the bottom layer. For model B this increase is 40%. This means that the bottom slow layer is required to counteract the effects of high shallower velocities in order to fit the data. Including structure of only the upper 13 layers (down to 125 km) of model A gives a misfit of 1.7 while that of model B gives 12.9 and is clearly inconsistent with our data.

Figure 11 shows the model obtained along the two–station leg 3–4. Shear velocities are significantly

higher than along station leg 1–8, by about 4.5% in the lithosphere and 6% in the asthenosphere at 150 km depth. Below about 70 km depth, velocities roughly follow those of PREM where the velocity increase at about 200 km is uncertain in our model. At nearly 4.8 km/s, the velocities found in the upper lithosphere are unusually high but are required to fit the dispersion curve in Figure 7. They are not unphysical and have been observed beneath the Canadian Shield (Grand and Helmberger, 1984) and in laboratory experiments (Jordan, 1979; Liebermann, 2000). The azimuth of the station leg is roughly aligned with past and present-day plate motion directions between 60 and 95°. Strong azimuthal anisotropy has been found in the Eastern Pacific Ocean (e.g. Montagner and Tanimoto, 1990; Larson et al., 1998; Laske et al., 1998; Ekström (2000)), and we find evidence that azimuthal anisotropy is about 3% in the southwestern part of our array, away from the Hawaiian Swell. The velocities shown here may therefore be those associated with the fast direction of azimuthal anisotropy though this would also include velocities in the asthenosphere where mantle flow is assumed to align anisotropic olivine.

The combined interpretation of all dispersion data shown in Figure 8 provides the final 3D model for isotropic velocity variations (Figures 12 and 13). While small-scale variations are most likely imaging artifacts caused by sparse path coverage, the most striking feature is a strong velocity gradient across the swell margin, starting at a depth of about 60 km, while the upper lithosphere is nearly uniform. The gradient amounts to about 1% across the array at 60 km depth but increases with depth to nearly 8% at 140 km depth. Along a profile across the swell margin we find clear evidence that the on-swell lower lithosphere has either been eroded from 90 to 60 km or has lower seismic velocities which is consistent with its rejuvenation by lithosphere–plume interaction. Our results appear in conflict with those of Priestley and Tilmann (1999) who find no evidence for lithospheric thinning along the Hawaiian Ridge. On the other hand, their model includes only two layers in the depth range shown here, the upper one being 75 km thick and representing the entire lithosphere. The velocity in their upper layer is 4.48 km/s which is lower than what we find in the upper 40 km but larger below that. Whether or not our model is consistent with an eroded lithosphere will be addressed in a later section but we clearly find some type of rejuvenation.

The base of the lithosphere is not defined in our modeling that does not explicitly include discontinuity kernels. But our suggestion of a doming lithosphere–asthenosphere boundary (LAB) is consistent with the results from a recent receiver function study that reaches into our array (Li et al., 2004). Their earlier study (Li et al. 2000) which samples the mantle beneath the island of Hawaii places the LAB at 120 km depth. Li et al. (2004) argue that the lithosphere thins away from the island of Hawaii and is only 50 km thick beneath Kauai, lending support for the hybrid dynamic support – lithosphere erosion model. Beneath a rejuvenated lithosphere we find a pronounced on-swell anomaly centered at 140 km depth in the asthenosphere. The anomaly could reach deeper than 200 km where our data lose resolution. This slow anomaly is consistent with

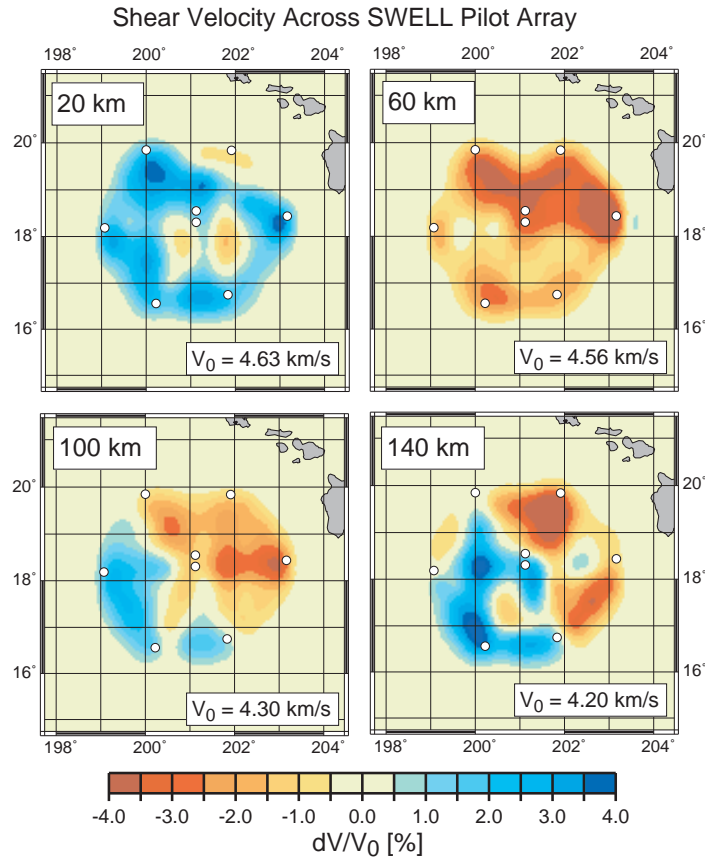


Fig. 12. Final three-dimensional model of shear velocity variation across the SWELL pilot array from the inversion of all two-station dispersion curves. Variations are shown at 4 depths and are given in per cent with respect to the velocities of the N&F model for 52-110Myr old lithosphere (given in the right bottom corner).

the asthenosphere identified by Priestley and Tilmann (1999) thought they give a somewhat lower velocity of 4.03 km/s. The anomaly found in the low-velocity body is about 4.5% slower than the off-swell, probably unaltered asthenosphere (our off-swell velocities are consistent with the velocities of PREM). Though not well resolved, our image suggests that we sense the bottom of the asthenosphere in the southwestern half of our array. Priestley and Tilmann (1999) placed the bottom of the asthenosphere at about 190 km depth beneath the Hawaiian islands though this is somewhat uncertain.

7 VALIDATION OF THE MODEL WITH OTHER APPROACHES

The two-station approach is appealing for several reasons. It readily provides path-averaged dispersion estimates along two-station legs without having to know details in earthquake source mechanisms. Having crossing paths available, it may provide detailed insight into lateral structural variations. Problems arise, how-

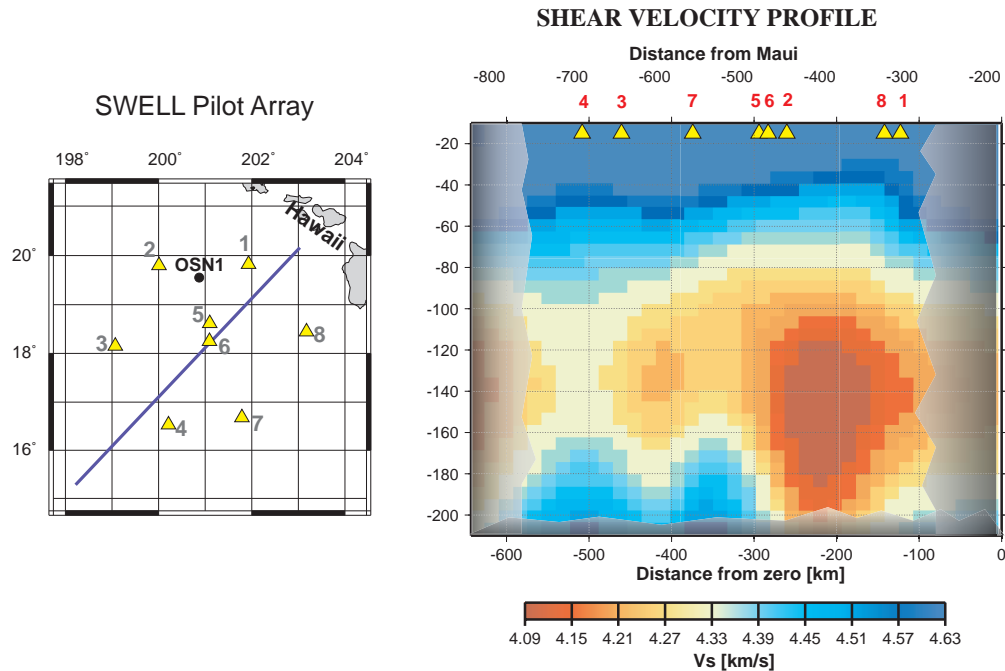


Fig. 13. Shear velocity profile across the 3D model of Figure 12. Velocities along the profile represent averages over velocities within 50 km of the profile. Imaging capabilities are reduced toward the end of the profile due to lack of data (e.g. the apparent thickening of the lithosphere east of sites # 1 and 8. Variations in the lithosphere and asthenosphere are clearly imaged. "Distance from zero" refers to the distance from the northeastern end of the line marked in the map.

ever, in cases where unmodeled effects become significant. These include off-great circle approach caused by lateral refraction between earthquakes and the array. We can validate our model by testing it against results when using the tripartite approach where we fit incoming spherical waves to the phase within station triangles. This is a low-resolution approach laterally but the advantage is that off-great circle propagation is included in the modeling and so may not bias the resulting model. The velocity maps in Figure 14a are significantly smoothed versions of the ones from the two-station method in Figure 8 but the basic features of velocity variations are consistent: there is a significant gradient across the swell margin and the gradient appears most pronounced at long periods. The fact that the velocity difference at 50s between triangles 3–4–6 and 1–8–6 is only 1.5% indicates that the extreme velocity differences must be confined to the edges of our array and likely extend beyond. The maps in Figure 14b indicate that errors are largest at long periods but the errors are small compared to observed variations. Since station #2 was operating only during the second deployment but all three stations have to provide a clean seismogram for a given earthquake, the number of earthquakes for triangles involving station #2 is reduced.

In the presence of azimuthal anisotropy, the velocities shown in Figure 14 represent true average isotropic

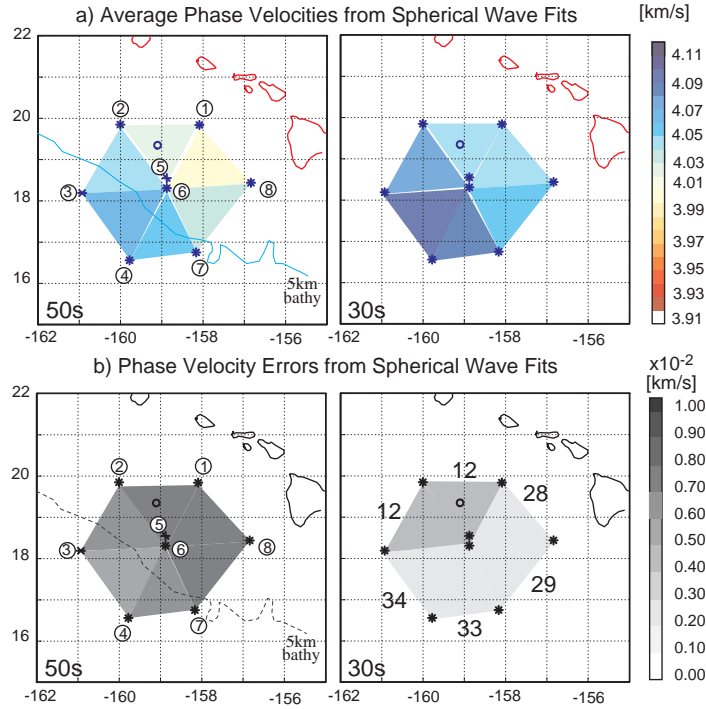


Fig. 14. a) Lateral phase velocity variations obtained with the station triangle method, at two periods. The maps are obviously smoothed versions of those in Figure 8 but the velocity gradient across the swell margin is still observed. b) Error maps. The errors are largest at long periods but remain below 0.007 km/s. The velocity gradient across the swell margin is therefore significant. The number of earthquakes used for each station triangle is given in the map for 30s.

velocities only in cases of good data coverage. We therefore check our results against inversions when azimuthal anisotropy is included in the modeling. The azimuthally varying phase velocity is parameterized as a truncated trigonometric power series,

$$c(\Psi) = c_i + a_1 \cos(2\Psi) + a_2 \sin(2\Psi) + a_3 \cos(4\Psi) + a_4 \sin(4\Psi) \quad (3)$$

where Ψ is the azimuth and the a_i are known local linear functionals of the elastic parameters of the medium (Smith and Dahlen, 1973; Montagner and Nataf, 1986) and c_i is the azimuth-independent average (or isotropic) phase velocity.

Solving Equation 3 is straightforward and in cases of adequate data coverage, the results for c_i should be consistent with those of Figure 14. Figure 15 shows that this is indeed the case for most of the periods considered, except at long periods where the number of reliable data decreases. When solving Equation 3 we search for 5 times as many unknowns as in the isotropic case. In cases of sparse data coverage, an inversion can yield anisotropic models that fit the data extremely well but are unnecessarily complicated

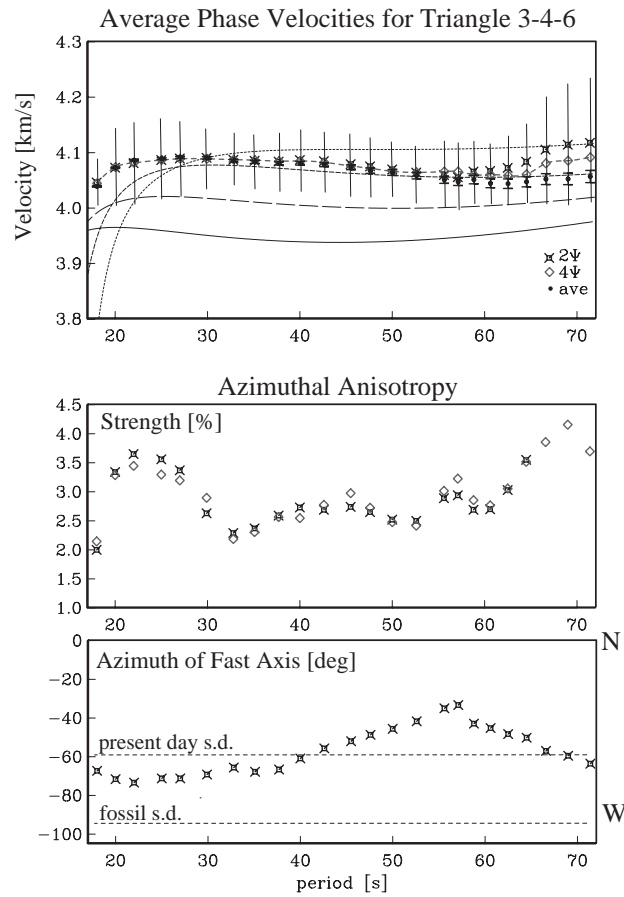


Fig. 15. Average phase velocities for station triangle 3–4–6. Shown are the results for the isotropic station triangle fit for Figure 14 as well as the c_i terms when fitting order 2 and 2/4 azimuthal anisotropy. Vertical bars mark the min/max variation of phase velocities in the 2Ψ fit. The N&F dispersion curves are shown for reference. Also shown are the strength of anisotropy obtained for the order 2 and 2/4 fits as well as the direction of fast phase velocity for the order 2 fit. Results agree overall, except at long periods where the number of constraining data decreases.

or physically unrealistic. Most realistic petrological models have one dominant symmetry axis that may be oriented arbitrarily in 3D space. For all such models, the contribution of the 4Ψ -terms is relatively small for Rayleigh waves. We see from Figure 15 that ignoring the 4Ψ -terms yields consistent results for c_i as well as the strength of anisotropy. The only time when results from anisotropic modeling including or excluding the 4Ψ -terms diverge is at long periods beyond 65 s where results are also different whether or not anisotropy is considered at all. In these cases of sparse data, ignoring strong azimuthal anisotropy yields biased values for c_i . On the other hand, with few data available the fits become uncertain, yielding phase velocity distributions that strongly oscillate with azimuth which is especially so for the 4Ψ -fits. Such strong variations have to be discarded as numerically unstable as well as unphysical. Overall the test here demonstrates that we obtain

reasonably unbiased velocities when we ignore anisotropy. The general good agreement of results when including azimuthal anisotropy in the modeling or not gives us confidence that the frequency-dependent phase velocities in this study and their implications for structure at depth are very well constrained. The modeling of the azimuth-dependence of phase velocity in terms of 3-D anisotropic structure is beyond the scope of this paper but preliminary modeling suggests that mantle flow in the asthenosphere follows the plate motion direction off the swell but is disturbed on the swell (manuscript in preparation).

Both the two-station as well as the triangle approach use only subsets of data. Due to the presence of noise or transient problems with individual stations, our database rarely contains earthquakes for which we can measure phase at all 8 stations. Both methods also strictly provide images within the array but give no information on structure outside of it though we have already discussed evidence that anomalies reach to the outside of our array. In a last consistency test, we embed our entire dataset of nearly 2000 phase measurements in our global database (Bassin et al., 2000). The global dataset includes nearly 20,000 high-quality hand-picked minor and major arc and great circle data and well as arrival angle data that enhance small-scale resolution (Laske and Masters, 1996). In a global inversion, contributions to our SWELL data from lateral heterogeneity between seismic sources and the array are implicitly included in the modeling. The highest frequency in our global dataset is currently 17 mHz which is near the long-period limit of the SWELL dataset. We choose 16 mHz (62.5s) for our test. All phase and arrival angle data are used in an inversion for a global phase velocity map that is parameterize in half-degree equal area cells. We use nearest neighbor smoothing in a least-squares iterative QR scheme (e.g. van der Sluis and van de Vorst, 1987). The resulting maps in Figure 16 clearly show that the SWELL data help image a low velocity region that is not resolved by the current global network of permanent seismic stations. With station KIP being until recently the only site in the area that has delivered high-quality data, not enough crossing rays are available to resolve structure at wavelengths much below 1000 km. The imaged velocity contrast between the deep ocean and the swell reaches 8% which is consistent with what we found with the two-station method. Being able to image structure outside of the array, we also notice that the low velocity anomaly extends well to the northeast of our array, most likely beyond the Hawaiian Islands. This is roughly consistent with Wolfe et al. (2002) who find a pronounced low-velocity anomaly extending from OSN1 to the Hawaiian Islands and from Oahu south to the northern end of the island of Hawaii. We are therefore confident that the results in our two-station approach are robust features and trace a profoundly altered lithosphere and asthenosphere beneath the Hawaiian Swell. A possible asymmetry of the low-velocity anomaly which is more pronounced to the southwest of Big Island than to the northeast is intriguing but is consistent with a similar asymmetry in bathymetry.

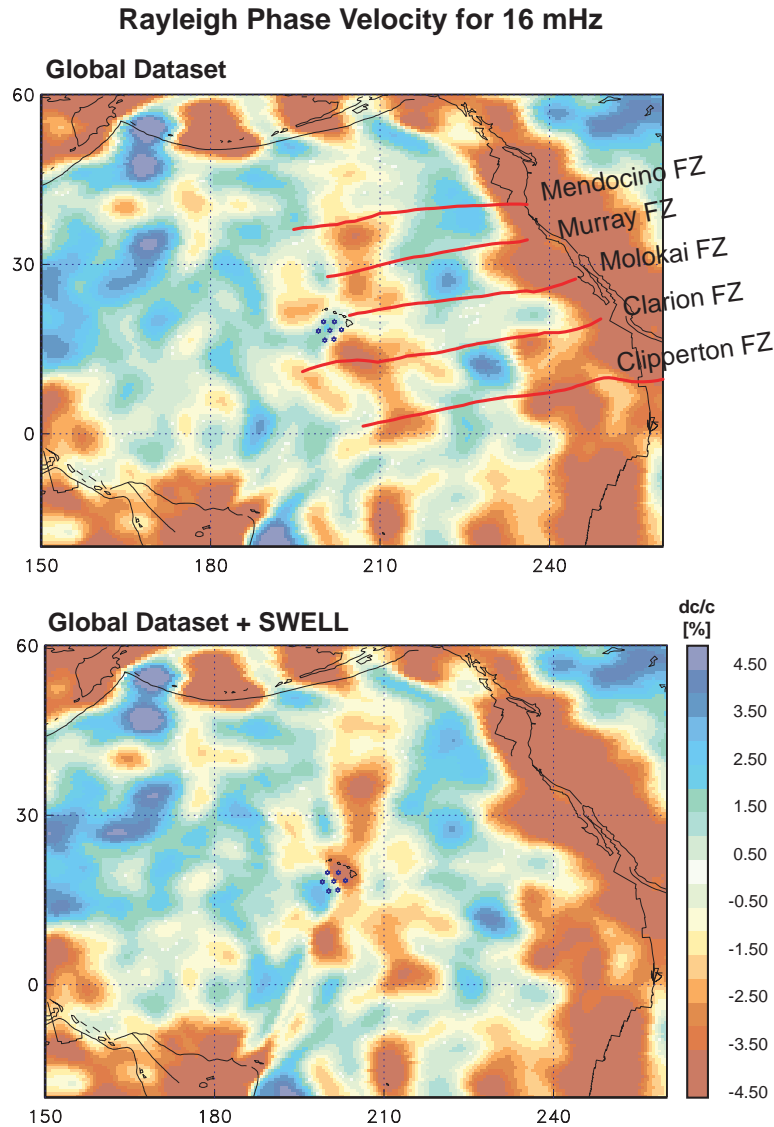


Fig. 16. North Pacific section of the global phase velocity map at 16 mHz obtained when inverting the global dataset only (top) and when including the SWELL data (bottom). Due to inadequate station distribution, the global dataset lack resolution near Hawaii. The SWELL data dramatically improve resolution and help image a low velocity region that extends from the SWELL array east beyond the islands.

8 DISCUSSION

8.1 Resolution Limits and Significance of Results

The skeptical reader may wonder if our data are precise enough to constrain the deep structure reliably. Our measurement errors increase at periods longer than 50s. The sensitivity kernel for 50 s Rayleigh waves to shear velocity at depth peaks around 80 km (GSA data repository electronic supplement ###, Appendix B).

However, this does not imply that our data cannot resolve deeper structure. Rather, the combination of all kernels at periods 50 s and shorter provides sensitivity beyond 100 km (see the Backus Gilbert test in GSA data repository electronic supplement ###, Appendix B). The rejuvenation of the lithosphere in Figure 13 is therefore extremely well constrained by our data because high precision data are required only at periods shorter than 30 s. Resolution below 120 km deteriorates somewhat, for three reasons: 1) the sensitivity kernels spread out over greater depths for longer periods, so deep structure is smeared out over a depth range greater than a few tens of km; 2) at periods longer than 50 s, the station spacing of 220 km is about a signal wavelength and measurement accuracy deteriorates; 3) at periods significantly beyond 60 s, ambient noise conditions for some earthquakes increases measurement uncertainties. We should stress however that our errors are most likely conservative compared to those of other studies (see Figure 7). We do not apply any smoothing or other conditioning along the dispersion curves but our errors are still less than 2%, which is a third of the anomaly found in the asthenosphere. The question arises whether this strong, possibly plume-related anomaly is required to fit our data. We had discussed in Figures 10 and 11 that the leg 1–8 dispersion curve would be marginally consistent with 1.7% higher velocities around 100km, with an associated 0.5% velocity reduction at 50 km depth. However, such a model would require unrealistically low velocities below 150 km. We have not found a model for leg 1–8 that exhibits velocities at 120 km depth as high as along leg 3–4 and infer that this anomaly is indeed real. On the other hand, asthenosphere velocities along leg 3–4 are PREM-like, i.e. near normal, and velocities cannot be lowered significantly. Flow-induced anisotropy along leg 3–4 could account for some the high off-swell velocity. This would lower the isotropic velocity contrast across the swell margin as there is no evidence that this flow extends to leg 1–8. The difference in anisotropy would lend support to a swell-scale mantle dynamical process.

8.2 Comparison with SWELL MT Data

During the first 7.5 months of the deployment, Constable and Heinson (2004) collected seafloor magnetotelluric data with a seven-station array that roughly overlapped with ours. The major features in their model include a resistive lithosphere underlain by a conductive lower mantle, and a narrow, conductive 'plume' connecting the surface of the islands to the lower mantle. They argue that their data require this plume, which is located just to the northwest of our array but outside of it. It has a radius of less than 100 km and contains 5-10% of melt. Unfortunately, our model does not cover this area. Constable and Heinson did not find any evidence for a lowering of shallow (60 km) resistivity across the swell and therefore argue against lithosphere reheating and thinning as proposed by Detrick and Crough (1978). In fact, resistivity appears to slightly increase in the upper 50 km. Due to the high resistivities found in the lithosphere (100-1000 Ω m), they place an

upper bound of 1% melt at 60 km depth where our lithosphere is thinnest and argue for a 'hot dry lithosphere' (1450-1500°C) compared to a cooler (1300°C) off-swell lithosphere. They estimate that a melt fraction of 3-4% could explain a 5% reduction in seismic velocities (Sato et al., 1989) but it would also reduce the resistivity to 10Ω which is not observed. Using temperature derivatives given by Sato et al. (1989), Constable and Heinson estimate that an increase of mantle temperature from 0.9 to 1.0 of the melting temperature (150-200 K in our case) can also cause a 5% velocity increase in our model but would not cause electrical resistivity to drop to 10Ω m. The authors therefore propose a thermally rejuvenated but not eroded lithosphere that would be consistent with both seismic and MT observations. On the other hand, the estimates of Sato et al. (1989) were obtained in high-frequency laboratory experiments and Karato (1993) argues that taking into account anelastic effects can increase the temperature derivatives for seismic velocities by a factor of 2. In this case, much smaller temperature variations are required to fit the seismic model. Constable and Heinson do not attempt to reconcile the seismic and MT model below 150 km depth but it is worth mentioning that their model exhibits a gradient to lower resistivity near the low-velocity body in the asthenosphere. Anelastic effects become most relevant at greater depths, below 120 km, when attenuation increases in the asthenosphere. As dramatic as our seismic model appears, it is nevertheless physically plausible. Modeling attempts that include thermal, melt and compositional effects reveal that no melt is required to explain our model below 120 km, while depletion through melt extraction could explain the lower velocities above it (Stephan Sobolev, personal communication).

8.3 Comparison with Bathymetry and Geoid

Both model parameterization and regularization used in the inversion influence the resulting velocity model, especially the amplitude of velocity anomalies. We can test the physical consistency of our model with other geophysical observables, such as the bathymetry in the region. Our test is based on the assumption that the regional lithosphere and asthenosphere is isostatically compensated, i.e. there is no uplift nor subsidence. We also assume that the causes for our observed velocity anomalies are predominantly of thermal origin in which case we can apply the velocity-density scaling of Equation 1 to convert δV_S to density variations. We assume Pratt isostasy and search for the optimum depth of compensation that is most consistent with observed lateral variations in bathymetry along the profile in Figure 13. We find that a compensation depth of about 130 km is most consistent with the observed bathymetry (Figure 17). Taking into account deeper structure grossly overpredicts variations in bathymetry while shallower compensation depths are unable to trace slopes in bathymetry. With a compensation depth of 130 km, the low-velocity anomaly in the asthenosphere would then give rise to uplift unless it is compensated by dense material further down. Katzman et

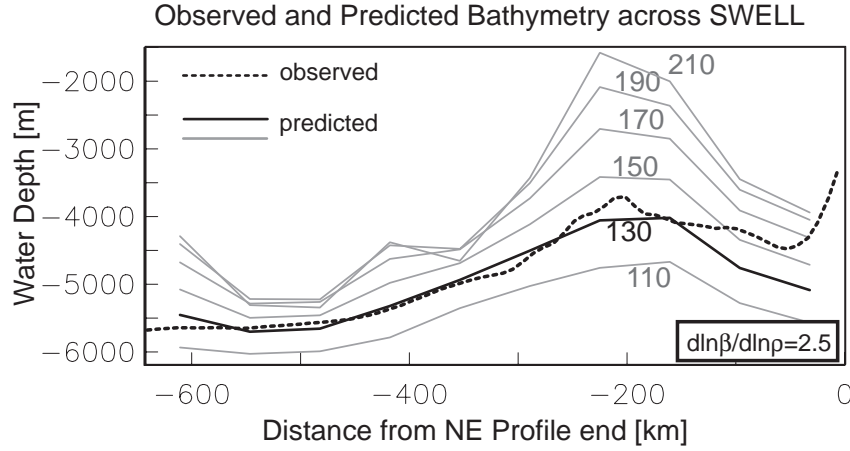


Fig. 17. Observed bathymetry along the profile marked in Figure 13. Also shown is the predicted bathymetry derived from the shear velocity model. We assume that the lithosphere is isostatically compensated above the compensation depth given by the labels at each curve. Assuming a deep compensation depth, we overpredict the bathymetry while a depth of about 130km matches it quite well. A shallower compensation depth is also inconsistent with the bathymetry.

al. (1998) argued that Hawaii is underlain by dense residue material that may be capable of sinking. On the other hand, the exact V_S -to- ρ scaling is relatively poorly known. Karato (1993) argues that anelastic and anharmonic effects significantly alter the temperature derivatives for velocity. In low-Q regions, such as the asthenosphere, the correction due to anelasticity roughly doubles. In this case, temperature anomalies as well as density anomalies have to be corrected downward, for a given shear velocity anomaly, or $d \ln V_S / d \ln \rho$ needs to be increased. In principle, we would need to reiterate our inversions using different scaling factors but here we only discuss the effects. Karato indicates that when taking anelastic and anharmonic effects into account $d \ln V_S / d \ln \rho$ decreases from roughly 4.4 at 100 km to 4.0 at 200 km. If we then assume an average scaling of 4.0 over the whole depth of our model, the predicted compensation depth deepens to 170 km, because shear velocity variations now have a reduced effect on bathymetry. This would include the anomaly in the asthenosphere without requiring compensating material at greater depth. We find no justifiable strategy to raise the compensation depth to 90 km or above that would be consistent with lithospheric thinning as proposed by Detrick and Crough (1978). Rather, the results here are roughly in agreement with the dynamic support model of Watts (1976) that places the compensation depth at 120 km.

We also test our model against the geoid. For Pratt compensation, the geoid anomaly, ΔN , is

$$\Delta N = \frac{-2\pi G}{g} \left\{ \int_0^h (\rho_w - \rho_0) z dz + \int_h^W (\rho(z) - \rho_0) z dz \right\} \quad (4)$$

where G is the gravitational constant, g acceleration of gravity, ρ_0 a reference density, h the water depth

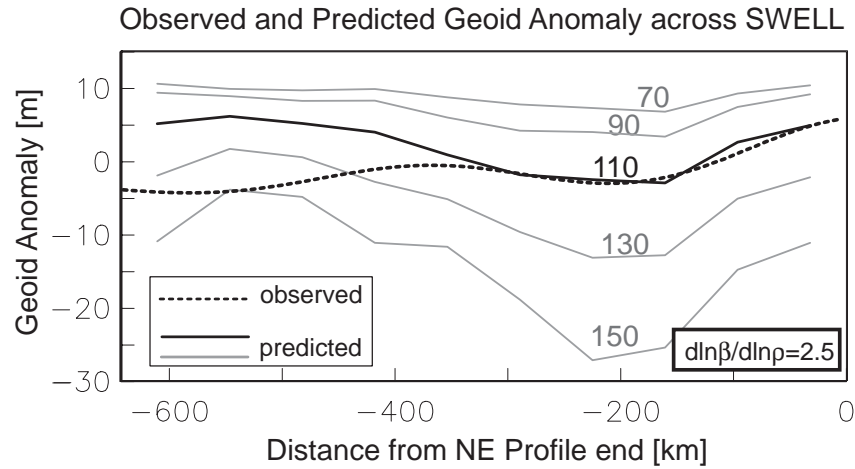


Fig. 18. Observed geoid anomalies from OSU91A1F. Only harmonic degrees $l = 3$ and above are considered. Also shown are geoid anomalies predicted from our model. The compensation depth for each curve is given by the label. Pratt isostatic compensation is calculated with respect to PREM. A baseline of 7m was added to the predictions to best match the geoid undulations between -400 and 0 km along the profile, since our data are insensitive to very long-wavelength structure.

and W the compensation depth. Equation 4 only holds if the area is isostatically compensated. We are somewhat cautious about this test because deeper structure in our model has now a graver impact than shallow structure but at the same time model errors are also greater. Figure 18 shows the observed geoid anomalies from OSU91A1F (Rapp et al., 1991) and the anomalies predicted from our velocity model. The exact base level caused by our model is somewhat uncertain because our data do not constrain structure of extremely long wavelength (e.g. harmonic degrees $l = 3$). As can be seen, taking into account structure above 110 km depth is most consistent with the geoid, east of the -400 km mark. A compensation depth of 120 km therefore appears roughly in agreement with both bathymetry and geoid which validates the approach assumed here. To the west of the -400 km, our model grossly overpredicts the geoid and we have no immediate explanation for this. Changing the velocity–density scaling relationship has only little impact overall and no impact at all on the optimal compensation depth. Our model implies an excess mass above 110 km, since lower compensation depths cause no changes. Velocity anomalies at great depth are somewhat uncertain but it is hard to find a compelling reason to conclude that velocities at shallower depths are wrong. Even if we assume that the model resulting from our two–station dispersion is biased toward fast velocities off the swell, the model from the tripartite method still implies the same overall inconsistency (low above the swell, high off the swell). As mentioned above, Katzman et al. (1998) find high velocities near Hawaii that correlate with a bathymetric and geoid high to the east of our profile mark -200 km. To the west of the -300 km mark they find a strong

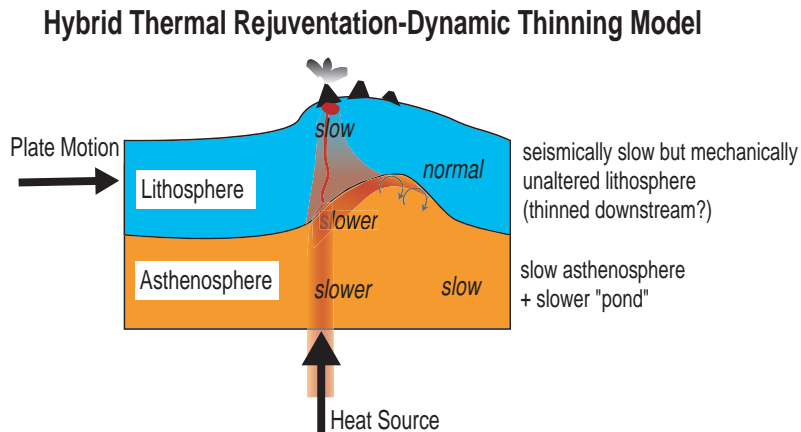


Fig. 19. Concept figure for a possible mechanisms for the Hawaiian swell that is most consistent with our data. The model is a hybrid thermal rejuvenation– dynamic support/thinning model. The lithosphere is rejuvenated by reheating but not mechanically eroded. The associated compensation depth would be 120 km. Mechanical thinning of the lithosphere may occur downstream, as proposed by Li et al. (2004), in an area that is not covered by our data.

negative anomaly in the mid–upper mantle that our technique is unable to image due to its depth. Such an anomaly would most likely compensate our shallow “excess mass”.

9 SUMMARY

During the 1997/1998 SWELL pilot experiment, we recorded Rayleigh waves on differential pressure sensors on the seafloor at an unprecedented signal level that allows us to image the lithosphere and asthenosphere beneath the Hawaiian Swell to depths beyond 150 km. The relatively inexpensive equipment is reliable in one–year deployments without significant maintenance.

We find pronounced lateral variations across the margin of the swell. In the deep ocean, velocities in the asthenosphere closely follow those of reference Earth model PREM, and are significantly higher than what is found along the island chain (Priestley and Tilmann, 1999). Velocities in the lid are higher than in PREM and also higher than in the Nishimura and Forsyth (1989) model for mature 100 Ma old lithosphere. Velocity variations along a profile across the swell margin suggest that the lithosphere on the swell has undergone a rejuvenation process.

Comparison of the velocities with those found in laboratory experiments and the results of a concurrent magnetotelluric study suggest that the anomalies are caused by thermal effects and that the amount of melt cannot exceed 1% in the altered lithosphere at 60 km depth. Our model is consistent with thermal rejuvenation and is in some disagreement with Priestley and Tilmann (1999) who find no significant rejuvenation beneath

the Hawaiian Islands. The seismic images bear the signature of a thermally rejuvenating lithosphere but our model is inconsistent with significant amounts of melt beneath the on-swell lithosphere, speaking against a mechanically eroded lithosphere that is proposed in the lithosphere thinning model (Figure 1), unless the thinning is restricted to within 100 km of the islands. The comparison with local bathymetry and the geoid shows that our model is inconsistent with a shallow compensation depth as implied by this model, at least in the area covered by our array. We find a deeper compensation depth as suggested by the dynamic support model but the latter does not account for the velocity variations we find in the lithosphere. If the area around Hawaii is isostatically compensated, we propose a hybrid thermal rejuvenation–dynamic thinning model in which the lithosphere near a possible plume head may be mechanically unaltered but thermally rejuvenated (Figure 19). This model could also explain seismic evidence found by Li et al. (2004) for thinning downstream, in an area that is not covered by our data.

Our data are inconsistent with the other models proposed for the Hawaiian Swell uplift and volcanism. The data lend no support for the compositional buoyancy model that requires high seismic velocities, unless plume–lithosphere interaction involves a very large area that extends well beyond the Hawaiian Swell. Off the swell, we find evidence for seismically fast material that is in conflict with the geoid, for compensation depths of 120 km or shallower. Katzman et al. (1998) find deeper low velocity anomalies in the upper mantle and it has been suggested that these are the signature of secondary shallow mantle convection. Lastly, our data are also inconsistent with a cracked lithosphere as the source of the Hawaiian volcanism as this model has no suggestion for the low–velocity anomaly found in the asthenosphere.

The SWELL pilot study covered only a small area of the Hawaiian Swell and cannot address some of the fundamental questions related to the possibly plume–related Hawaiian volcanism. Rayleigh waves are extremely useful tools to investigate the shallow (less than 200 km) lithosphere–asthenosphere system which remains elusive to standard teleseismic body wave tomography. On the other hand, fundamental mode Rayleigh waves in the period range shown here do not constrain structure in the transition zone. Unlike the analysis of receiver functions, our surface wave analysis cannot support or disprove the lower mantle origin of a proposed mantle plume. SWELL is now part of PLUME (Plume–Lithosphere–Undersea–Mantle Experiment) (Laske et al., 2006). This experiment involves the occupation of 10 land and 70 ocean bottom sites that are well distributed over a 1000 km wide area around Hawaii. The combination of all techniques mentioned above will give us the unprecedented opportunity to collect excellent seismic constraints that will help us resolve one of the most tantalizing questions in plate tectonics: is the Hawaiian hot spot volcanism fed by a deep–seated mantle plume or not?

ACKNOWLEDGMENTS

We wish to thank the L-CHEAPO team at IGPP (Cris Hollinshead, Paul Zimmer and Dave Willoughby) for making this experiment possible. The team deployed and recovered the instruments on U. Hawaii's R/V Moana Wave. We thank the officers and crew of this vessel for three excellent cruises. The operators of OSN1, GEOSCOPE, GSN, IRIS and its data management center provided data and instrument responses used in this study. Many thanks go to Stephan Sobolev for his thermo-mechanical calculations for our model. Laske wishes to thank Dave Sandwell and Jerry Winterer for numerous fruitful discussions. Reviews by Walter Zürn and Zhijun Du, and editors Gillian Foulger and Donna Jurdy are greatly appreciated and helped to improve this manuscript. This research was financed by National Science Foundation grants OCE-95-29707 and OCE-99-06836.

10 GSA DATA REPOSITORY ELECTRONIC SUPPLEMENT ###, APPENDIX A: DESCRIPTION OF THE FIELD PROGRAM

The field program began in April 1997 with the deployment of 8 L-CHEAPO instruments in a hexagonal array (Figure 2) during a 7-day cruise on the 210-foot University of Hawaii R/V Moana Wave. The instruments were deployed at water depths ranging from 4400 m to 5600 m. Two instruments were placed at the center of the hexagon, at a distance of about 25 km, in order to attain full lateral resolution in case one instrument should fail. This first deployment also included 8 magnetotelluric (MT) ocean bottom instruments and one on land (Constable and Heinson, 2004). In December 1997, we recovered all 16 instruments during a 8-day cruise and re-deployed the 8 L-CHEAPOs after replacing the lithium batteries. The re-deployment allowed the SWELL pilot array to be contemporaneous with the planned but postponed OSN1 borehole test (Dziewonski et al., 1991). The final recovery was in early May 1998 on a 5.5-day cruise. Regarding the 16 L-CHEAPO drops, all were recovered and all but 3 produced continuous 25Hz data streams for the whole period of deployment. In both deployments, the failing instrument was at one of the central sites where we prudently had a backup instrument. The instrument at site 2 failed initially after recording for roughly two weeks. During the re-deployment cruise in December 1997, we were able to repair it, and it then performed flawlessly after the second drop.

In the configuration used in the SWELL pilot experiment, the L-CHEAPO instruments had a 16-bit data logging system that was controlled by an Onsett Tattletale 8 (Motorola 68332) microcomputer. The 162 dB dynamic gain ranging operated flawlessly, except for the failing instrument at site number 5. The data were stored on 9-Gbyte SCSI disks in the logger. Due to the relatively small data volume of roughly 1 Gbyte per 6 months we used no data compression. Three McLean glass balls provided floatation while a roughly 1-ft

tall piece of scrap metal served as ballast to keep the instrument on the ocean floor. Communication with the instrument was established through an Edgetech acoustic system with coded signals for disabling, enabling and for releasing the instrument from the ballast through a burn wire system. A flag and a strobelight helped locate the surfaced instrument during day and night recoveries. The datalogger was timed by a custom low-power Seascan oscillator built for SIO with a nominal timing accuracy of about 5×10^{-8} correctable for drift to 0.1 s/yr. The datalogger clocks were synchronized with GPS time before deployment and compared with it after recovery. The average total clock drifts were 700 ms during the first deployment and 250 ms during the second, resulting in an average drift of 75 ms/month (or 0.9 s/yr). We applied linear clock drift corrections to the data though timing errors of this magnitude are irrelevant for our study.

11 GSA DATA REPOSITORY ELECTRONIC SUPPLEMENT ###, APPENDIX B: THE DEMANDS ON SEISMIC BANDWIDTH AND THE USE OF DPGS

Though relatively cost-effective, the choice to deploy Cox-Webb differential pressure gauges (DPGs) (Cox et al., 1984) appeared somewhat disappointing prior to our pilot deployment as a pressure sensor does allow us to observe shear wave splitting and converted phases from discontinuities, or record Love waves. The observation of the latter on the ocean floor has so far been extremely rare due to prohibitive noise levels on horizontal seismometer components. There has also been some concern that the effects of ocean noise from infragravity waves are much larger in pressure, recorded by the DPG, than in ground motion, recorded by a seismometer (Webb, 1998). And finally, the Pacific Ocean is found to be much noisier than the Atlantic Ocean, due to stronger storm activity, though this may affect only signals at periods shorter than considered in our study. On the other hand, infragravity noise levels may depend on water depth and the deep ocean environment around Hawaii could allow us to collect data at more favorable signal levels than elsewhere.

Surface wave phase velocity is sensitive to shear and compressional velocity, V_S (or β) and V_P (or α), as well as density, ρ :

$$\frac{\delta c}{c} = \int_0^a r^2 dr (\tilde{A} \cdot \delta\alpha + \tilde{B} \cdot \delta\beta + \tilde{R} \cdot \delta\rho). \quad (5)$$

For periods relevant to this study, Rayleigh waves are most sensitive to V_S between 30 and 140 km though sensitivity extends beyond 200 km, if reliable measurements are available at 90 s and beyond (Figure 20). Rayleigh waves are also quite sensitive to V_P from the crust downward to about 60 km. The great similarity in sensitivity kernels does not allow us to obtain many independent constraints to resolve V_P very well. To explore the lithosphere-asthenosphere system and the causes for the Hawaiian Swell uplift, we need to image structure to depths beyond 150 km, preferably down to at least 200 km. A Backus-Gilbert analysis (Backus

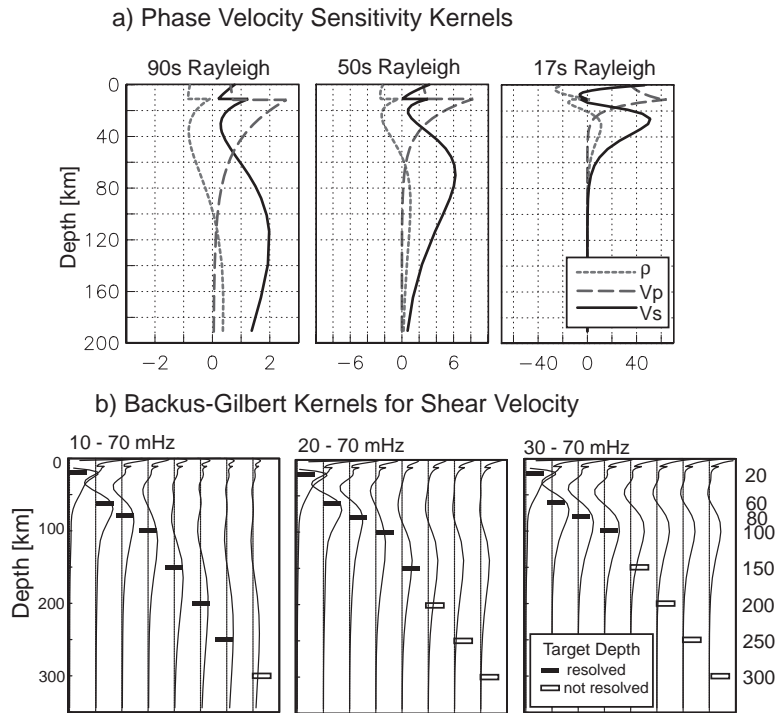


Fig. 20. a) Rayleigh wave sensitivity to structure at depth, shown at three periods. At a given period, sensitivity is greatest for deep shear velocity, V_S , but sensitivity for shallow compressional velocity, V_P is also significant. Sensitivity to density, ρ is less but needs to be accounted for properly in an inversion.

b) Backus–Gilbert kernels for Rayleigh waves, for three frequency ranges and a given model error of 1%. The 8 kernels represent the recovery of a delta function at 8 given target depths (numbers on the right hand side). With dispersion data as low as 10 mHz, structure down to 250 km depth can be resolved. Even a dataset limited to frequencies above 30 mHz is able to recover structure down to 100 km.

and Gilbert, 1968) gives us insight into what bandwidth the observed Rayleigh waves need to have in order to resolve as best as possible a delta function–shaped anomaly at a given target depth. The trade-off between the desired error in the model and the width of the recovered delta function (spread) does not allow us to resolve arbitrarily fine details. Figure 20 shows over which depth range an input delta function is smeared out, after choosing the optional linear combination of data kernels (Figure 20a) for an inversion. Shallow structure is spread over a relatively narrow range but structure below 100 km can be spread out over 100 km or more. We find that with dispersion data between 10 and 70 mHz (100–14 s period), we start to lose recovery of structure beyond about 270 km depth. While it is straightforward to attain this level of resolution with observations on land, ocean noise probably prohibits the observation of surface waves near 10 mHz. With data between 20 and 70 mHz (50–14 s), which was near the limit of what has been achieved in the MELT experiment, recovery of structure just beyond 150 km is possible. Imaging capabilities dramatically deteriorate when the

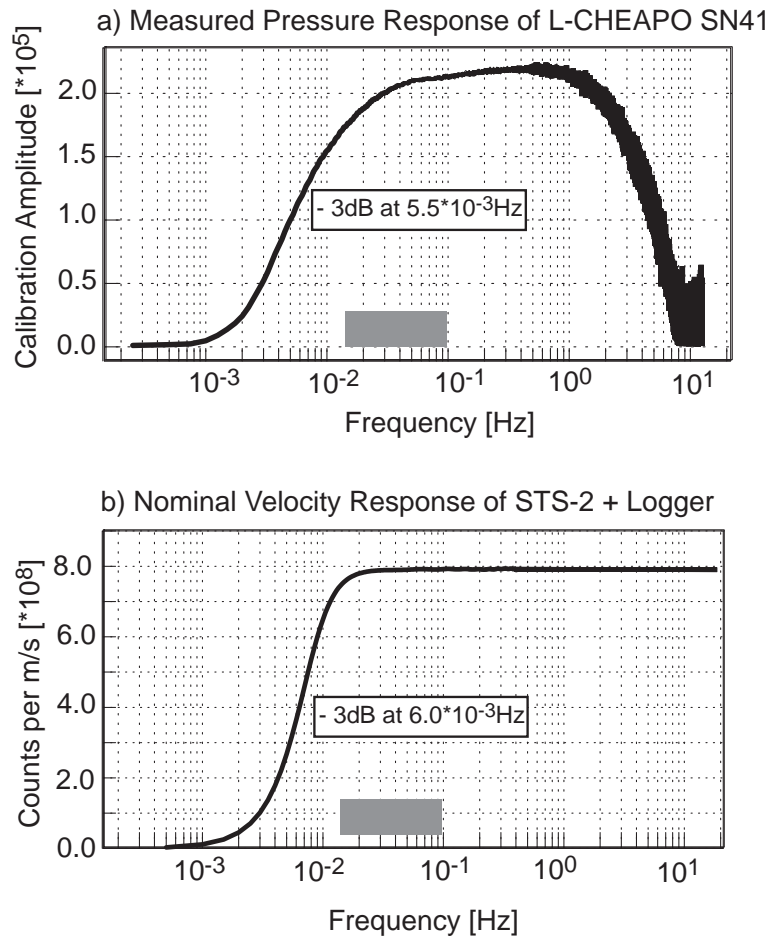


Fig. 21. a) Measured pressure response of one of the L-CHEAPO packages (site #6 in deployment 1 and site #7 in deployment 2). The calibration amplitude was arbitrary but the frequency–dependence was determined reliably and scales to Volts/PSI.

b) Nominal instrument response of an STS-2/Reftek 24-bit package as is deployed at the Anza array (<http://eqinfo.ucsd.edu/deployments/anza.html>). The instrument response was obtained from the DATALESS SEED volume distributed by the IRIS DMC (Incorporated Research Institutions for Seismology Data Management Center). The -3dB points of the two responses are quite compatible.

bandwidth is reduced to frequencies above 30 mHz (30 s). In this case, structure much beyond 100 km is not recovered.

Traditional OBS equipment uses seismometers with resonance frequencies around 1s, for example the Mark L4-3D that has been used in active seismic source experiments on land and in the oceans. We prefer to use a sensor with greater bandwidth that does not necessitate elaborate signal–enhancing procedures. At the time of the SWELL pilot deployment, the Cox–Webb DPG appeared to be a cost–effective alternative.

Figure 21 compares the pressure response of the DPG package as determined during a laboratory calibration test prior to the deployment, after the instrumentation was fine-tuned to extend the bandwidth at low frequencies. For comparison, we also show the ground velocity response of a broadband Wielandt–Streckeisen STS-2 seismometer package that is often used during temporary and long-term deployments on land. The DPG compares quite favorably though its roll-off at long periods is somewhat faster than for the STS-2. The absolute sensitivities of the instruments were not determined during the calibration test. We could probably determine these a posteriori by comparing a variety of seismic and noise signals but this is irrelevant and beyond the scope of this project. Not shown is the phase response that was tested to be within $\pm 0.5\%$ between all instruments, except for a linear phase shift that was induced in the test due to uncertainties in the onset times of the input signal. The dispersion measurement errors are typically of the same order. Since the calibration tests are subject to some error, and the effects of ground coupling of the instruments on the ocean floor are unknown we saw no benefit in correcting the raw seismograms for instrumental effects.

12 GSA DATA REPOSITORY ELECTRONIC SUPPLEMENT ###, APPENDIX C: EFFECTS FROM SHALLOW STRUCTURE

In the period range analyzed here, surface waves are quite sensitive to crustal structure without being able to resolve details. We therefore take crustal effects into account in a starting model. The crustal structure in our study area is not known in great detail. The most profound difference between the crust on the islands and in the oceans is its thickness which has a significant effect. Information on crustal structure of the islands, especially the island of Hawaii, comes from refraction seismic and teleseismic work. In refraction seismic work on the north flank of Kilauea, the crust was found to have 3 principal layers (Ryall and Bennett, 1968). A 1.2–2.5 km thick layer with $V_P = 3$ km/s – thought to be a series of fractured vesicular lava flows – is underlain by a 4–6 km thick layer with $V_P = 5.3$ km/s (principal volcanic layer) and a 6–7 km thick layer with $V_P = 7$ km/s (principal layer of oceanic crust). A more comprehensive seismic refraction study with sea shots surrounding the island (Hill, 1969) found similar velocities on the southwest flanks of Kilauea. On average, Hill found a two-layer crust beneath the island where a 4–8 km thick layer with V_P increasing from 1.8–3.3 km/s near the top to 5.1–6.0 km/s near the bottom (accumulated pile of lava flows) is underlain by a 4–8 km thick basal layer with $V_P = 7.0 - 7.2$ km/s (original oceanic crust plus intrusive systems) though the crust may be as thick as 20 km beneath Mauna Kea and Kohala Mountain. Hill also pointed out that early arrivals associated with the summits of Kilauea and Mauna Loa suggest shallow (2–3 km) high velocities ($V_P = 7.0$ km/s). Shallow high-velocity bodies (3–5 km depth) were also found beneath Mauna Kea and Kohala Mountain. Hill and Zucca (1987) argued that these bodies represent the upper crustal magma

Table 1. Crustal model used in this study. V_S and V_P are simplified versions of the crustal structure along the ESP 1 profile (Lindwall, 1991), near OSN1.

Layer	Thickness [m]	V_P [km/s]	V_S [km/s]	ρ [g/cm ³]
water	5000	1.50	0.00	1.03
sediments	200	2.00	0.5	1.50
Layer 2A	1300	5.30	3.00	2.50
Layer 2B	2000	6.40	3.70	2.80
Layer 3	3000	7.00	3.90	2.90
Mantle	–	8.19	4.63	3.35

storage complexes. Teleseismic studies by Ellsworth and Koyanagi (1977) and Okubo et al. (1997) revealed that the crust beneath the summit and two radial rifts were confirmed to have anomalously high velocities ($V_P = 6.4$ to 7.0 km/s) in contrast to the nonrift areas where velocities between 5.0 and 6.0 km/s can be found. There is no evidence for significant partial melt (5%) down to at least 40km.

The crustal structure of the islands is quite different from that of the surrounding ocean. Early work by Raitt (1956) northeast of the island of Hawaii, on the island side of the moat, revealed a two-layered, 7 km thick crystalline crust covered by 240 meters of sediments. The parameters of the crystalline layers were given as 2.3 km thick with $V_P = 4.3$ km/s and 4.7 km thick with $V_P = 6.6$ km/s. Shor (1960) collected refraction seismic data across a flat bank at Gardner Pinnacles, roughly 900 km to the northwest of Kauai. He found the crust to be 17 km thick on the Hawaiian ridge but the crust thins to 5km within 190km of the ridge. The velocities found in the two-layer crystalline crust are slightly higher than those found by Raitt (4.7 km/s and 6.9 km/s). Surveys more closely tied to our own study area include the wide-angle refraction and multi-channel seismic studies of Watts et al. (1985), Brocher and ten Brink (1987), and Lindwall (1988) for which about 15 sonobuoy and expanding spread profiles (ESP) were deployed in a corridor roughly perpendicular to the Hawaiian Ridge, passing through the Kaiwi Channel between Oahu and Molokai. The southwestern end of the corridor was near the OSN1 borehole. Brocher and ten Brink (1987) found normal oceanic crust away from the islands. The velocity structure varies along the corridor but the authors summarize the structure in three principal layers. The top layer includes pelagic sediments ($V_P = 1.5 - 1.7$ km/s) in the top 250 m and volcanic clasts to depths up to 2700m ($V_P = 3.7 - 4.4$ km/s), close to the islands. Their initial assessment of sedimentary cover through two-way travel times indicated a cover of 250 m away from the islands, and about 1km in the Hawaiian Moat (see Figure 2) but the latter was corrected upward, after including first arrival phases in the modeling. A sedimentary cover of 243 m was later found at the OSN1 borehole (Dziewonski et al., 1991). Layer 2 and 3 represent the igneous crust. Velocities in layer 2 increase from 4.5 to 6.5 km/s for V_P and from 2.2–3.5 km/s for V_S . Velocities in layer 3 increase from 6.5 to 7.0 km/s for V_P and from 3.5

to 3.8 km/s for V_S . Brocher and ten Brink (1987) reported that the velocities in layer 2 are normal far away from the Hawaiian Arch but are significantly lower, by up to 0.9 km/s, in the vicinity of the arch, near the northeastern end of our array. Lindwall (1988) reported the results of two 60-80 km long ESP profiles in the Kaiwi Channel and in the Kauai Channel between Oahu and Kauai. He found the crust there to be 16 km thick, with a 4 km thick sedimentary cover ($V_P = 3.5 - 4.2$ km/s) and a 5 km thick layer comprising the main volcanic edifice ($V_P = 5.0 - 6.4$ km/s) overlying a normal, 7 km thick oceanic crust. Lindwall (1991) analyzed profile ESP1, which is close to the OSN1, in greater detail. He refined the earlier model to include updated estimates of Q , a series of seismically fast layers at 3 km depth and a 1km transition to the mantle.

We use Lindwall's (1991) model to construct our 4-layer crustal reference model (Table 1). Density constraints come from the OSN1 borehole (Collins et al., 1991) and standard scaling relationships. We choose a sedimentary cover of 200 m. This is lower than what is found at OSN1. On the other hand, sediment maps of the area, suggest an average of no more than 150m (Renkin and Sclater, 1988). The effect of such a difference in thickness on Rayleigh wave phase velocity is insignificant. There is no evidence that crustal structure varies significantly across the SWELL pilot array other than that velocities in layer 2 may be low in the northeast corner (station triangle 2-1-8), though the extent of this is uncertain. Figure 22 shows that phase velocities between 20 and 40s are affected somewhat though such changes in velocities are within measurement uncertainties. Figure 22 also shows effects of extreme variations in crustal structure that are most likely irrelevant for the study within our array but need to be considered when comparing our model with models determined using island stations. When increasing the sediment thickness to 1km the phase velocities are reduced overall, but notably only for periods shorter than 40 s. These changes may be barely larger than measurement uncertainties. On the other hand, a thickening of oceanic layer 3 by 10 km significantly shifts the whole phase velocity curve downward, in the period range shown. Effects are enhanced by lowering crustal velocities to match those found beneath the islands. Locally, the most relevant effects for this study are most likely due to variations in water depth where only periods shorter than 30 s are affected significantly. In practice, the impact of water depth are obscured by path-averaging along two-station legs though we take changes in water depth into account.

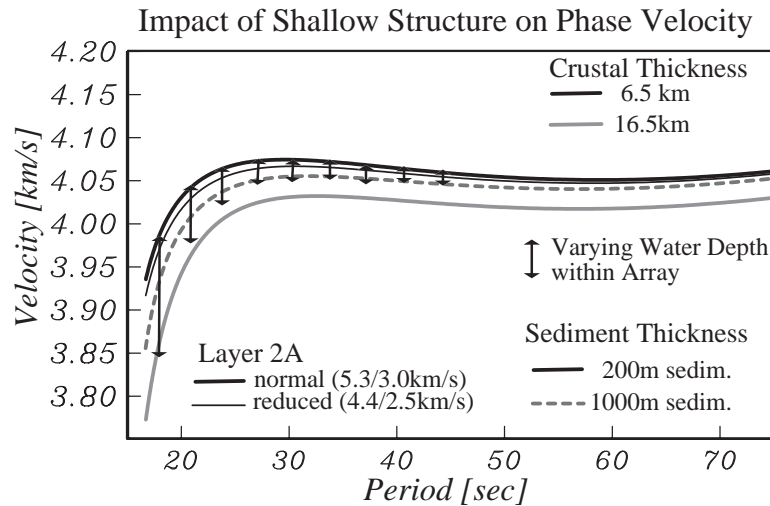


Fig. 22. The impact of variations in shallow structure on Rayleigh wave phase velocities. The reported lowering of velocities in layer 2 by 0.8 km/s (V_P) and 0.5 km/s (V_S) has an insignificant impact. Assumed, but not observed differences in sediment thickness by 800 m have a barely significant impact. On the other hand, a thickening of oceanic crust by 10 km lowers the whole dispersion curve by about 0.7%. Local differences in water depth (4350 m at site #1 to 5600 m at site #4) change phase velocities significantly only at periods shorter than 30 s, by up to 0.7%. The effects of any path-averaged water depth lie in between.

13 REFERENCES

- Alsina, D. and Snieder, R., (1993), A test of the great circle approximation in the analysis of surface waves. *Geophys. Res. Lett.*, 20, 915–918.
- Anderson, O.L., Schreiber, E., Liebermann, R.C. and Soga, M., (1968), Some elastic constant data on minerals relevant to geophysics. *Rev. Geophys.*, 6, 491–524.
- Anderson, O.L. and Isaak, M., (1995), Elastic constants of mantle minerals at high temperature. in: *Mineral Physics and Crystallography, AGU Ref. Shelf # 2*, ed. T.J. Ahrens, 64–97.
- Backus, G. and Gilbert, F., (1968), The Resolving Power of Gross Earth Data. *Geophys. J.R. astr. Soc.*, 16, 169–205.
- Bassin, C., Laske, G. and Masters, G., (2000), The Current Limits of Resolution for Surface Wave Tomography in North America. *EOS Trans. AGU*, 81, F897.
- Brocher, T.M. and ten Brink, U.S., (1987), Variations in Oceanic Layer 2 Elastic Velocities Near Hawaii and Their Correlation to Lithosphere Flexure. *J. Geophys. Res.*, 92, 2647–2611.
- Collins, J. A., Duennebie, F. and Shipboard Science Party, (1991), Site survey and underway geophysics. *Proceedings of the Ocean Drilling Program, Vol 136/137*, 27–36.

Collins, J. A., Vernon, F.L., Orcutt, J.A., Stephen, R.A., Peal, K.R., Wooding, F.B., Spiess, F.N., and Hildebrand, J.A., (2001), Broadband Seismology on the oceans: Lessons from the Ocean Seismic Network Pilot Experiment. *Geophys. Res. Let.*, 28, 49–52.

Constable, S. and Heinson, G., (2004), Hawaiian hot–spot swell structure from seafloor MT sounding. *Tectonophys.*, 389, 111–124.

Cox, C., Deaton, T. and Webb, S., (1984), A Deep–Sea Differential Pressure Gauge. *J. Atmos. Oceanic Technol.*, 1(3), 237–346.

Crough, S.T., (1978), Thermal origin of midplate hot–spot swells. *Geophys. J.R. astr. Soc.*, 55, 451–469.

Davies, G.F., (1988), Ocean bathymetry and mantle convection, 1: large–scale flow and hotspots. *J. Geophys. Res.*, 93, 10,467–10,480.

Detrick, R.S. and Crough, S.T., (1978), Island Subsidence, Hot Spots, and Lithospheric Thinning. *J. Geophys. Res.*, 83, 1236–1244.

Dziewonski, A.M., and Anderson, D.L., (1981), Preliminary reference Earth model. *Phys. Earth Planet. Inter.*, 25, 297–356.

Dziewonski, A., Wilkens, R.H., Firth, J.V. and Shipboard Science Party, (1991), Background and Objectives of the ocean seismographic network, and leg 136 drilling results. *Proceedings of the Ocean Drilling Program, Vol 136/137*, 3–8.

Ekström, G, Tromp, J. and Larson, E., (1997), Measurements and global models of surface wave propagation. *J. Geophys. Res.*, 102, 8137–8157.

Ekström, G., (2000), Mapping the Lithosphere and Asthenosphere With Surface Waves: Lateral Structure and Anisotropy. in: "The History and dynamics of Global Plate Motions", M.A. Richards, R.G. Gordon and R.D. van der Hilst (eds), *Geophys. Monograph, Vol. 121, AGU, Washington D.C.*, 239–255.

Ellsworth, W.L. and Koyanagi, R.Y., (1977), Three–Dimensional Crust and Mantle Structure of Kilauea Volcano, Hawaii. *J. Geophys. Res.*, 82, 5379–5394.

Forsyth, D.W., Weeb, S.C., Dorman, L.M. and Shen, Y., (1998), Phase Velocities of Rayleigh Waves in the MELT Experiment on the East Pacific Rise. *Science*, 280, 1235–1238.

Friederich, W., Wielandt, E. and Stange, S., (1994), Non–plane geometries of seismic surface wavefields and their implications for regional surface–wave tomography. *Geophys. J. Int.*, 119, 931–948.

Grand, S.P. and Helmberger, D.V., (1984), Upper mantle shear structure of North America. *Geophys. J.R. astr. Soc.*, 76, 399–438.

Grand, S., van der Hilst, R.D. and Widiyantoro, S., (1997), Global seismic tomography: a snapshot of convection in the Earth. *GSA Today*, 7, 1–7.

Hill, D.P., (1969), Crustal structure of the island of Hawaii from seismic–refraction measurements. *Bull. Seism. Soc. Am.*, 59, 101–130.

Hill, D.P. and Zucca, J.J., (1987), Geophysical constraints on the structure of Kilauea and Mauna Loa Volcanoes and some implications for seismomagmatic processes. in: "Volcanism in Hawaii", R.W. Decker, T.L. Wright and P.H. Stauffer (eds), U.S. Geological Survey Professional Paper; 1350, 903–917.

Jordan, T.H., (1979), Mineralogies, densities, and seismic velocities of garnet lherzolites and their geophysical implications. in: "The Mantle Sample: Inclusions in Kimberlites and Other Volcanics, Vol 2.", F.R. Boyd and H.O.A. Meyer (eds), AGU, Washington DC, 1–14.

Karato, S., (1993), Importance of anelasticity in the interpretation of seismic tomography. *Geophys. Res. Lett.*, 20, 1623–1626.

Katzman, R. Zhao, L. and Jordan, T.H., (1998), High–resolution, two–dimensional vertical tomography of the central Pacific mantle using *ScS* reverberations and frequency–dependent travel times. *J. Geophys. Res.*, 103, 17,933–17,971.

Keyser, M., Ritter, J.R.R., Jordan, M., (2002), 3D shear–wave velocity structure of the Eifel Plume, Germany. *Earth Planet. Sci. Lett.*, 203, 59–82.

Larson, E.W.F., Tromp, J. and Ekström, G., (1998), Surface–wave polarization data and global anisotropic structure. *Geophys. J. Int.*, 132, 654–666.

Laske, G. and Masters, G., (1996), Constraints on global phase velocity maps by long–period polarization data. *J. Geophys. Res.*, 101, 16,059–16,075.

Laske, G. and Masters, G., (1998), Surface–wave polarization data and global anisotropic structure. *Geophys. J. Int.*, 132, 508–520.

Laske, G., Phipps Morgan, J. and Orcutt, J.A., (1999), First Results from the Hawaiian SWELL Pilot Experiment. *Geophys. Res. Lett.*, 26, 3397–3400.

Laske, G., Collins, J.A., Wolfe, C.J., Weeraratne, D., Solomon, S., Detrick, R.S., Orcutt, J.A., Bercovici, D.A. and Hauri, E.H., (2006), The Hawaiian PLUME Project Successfully Completes its First Deployment. *EOS Trans. AGU*, 87 Fall Suppl., V13B-0657.

Li, X., Kind, R., Yuan, X., Wölbern, I. and Hanka, W., 2004, Rejuvenation of the lithosphere by the Hawaiian plume. *Nature*, 427, 827–829.

Li, X., Kind, R., Priestley, K., Sobolev, S.V., Tilmann, F., Yuan, X. and Weber, M., (2000), Mapping the Hawaiian plume with converted seismic waves. *Nature*, 405, 938–941.

Liebermann, R.C., (2000), Elasticity of Mantle Minerals (Experimental Studies). in: "Earth's Deep Interior; Mineral Physics and Tomography From the Atomic to the Global Scale", S-I. Karato, A.M. Forte,

R.C. Liebermann, G. Masters and L. Stixrude (eds), *Geophysical Monograph 117*, AGU, Washington DC, 181–199.

Lindwall, D.A., (1988), A Two-Dimensional Seismic Investigation of Crustal Structure Under the Hawaiian Islands Near Oahu and Kauai. *J. Geophys. Res.*, 93, 12,107–12,122.

Lindwall, D.A., (1991), Old Pacific Crust Near Hawaii: A Seismic View. *J. Geophys. Res.*, 96, 8191–8203.

Maggi, A., Debayle, E., Priestley, K. and Barruol, G., (2006), Multimode surface waveform tomography of the Pacific Ocean: a closer look at the lithospheric cooling signature. *Geophys. J.Int.*, 166, 1384–1397.

Maupin, V., (1992), Modelling of laterally trapped surface waves with application to Rayleigh waves in the Hawaiian swell. *Geophys. J. Int.*, 110, 553–570.

Montagner, J.-P. and Nataf, H.-C., (1986), a simple method for inverting the azimuthal anisotropy of surface waves. *J. Geophys. Res.*, 91, 511–520.

Montagner, J.-P. and Tanimoto, T., (1990), Global anisotropy in the upper mantle inferred from the regionalization of phase velocities. *J. Geophys. Res.*, 95, 4797–4819.

Montelli, R., Nolet, G., Dahlen, F.A. and Masters, G., (2006), A catalog of deep mantle plumes: new results from finite-frequency tomography. *Geochem. Geophys. Geosys.*, in press .

Moore W.B., Schubert, G. and Tackley, P., (1998), Three-dimensional Simulations of PLume–Lithosphere Interaction at the Hawaiian Swell. *Science*, 279, 1008–1011.

Morgan, W.J., (1971) Convection plumes in the lower mantle. *Nature*, 230, 42–43.

Müller, R.D., Roest, W.R., Royer, J.-Y., Gahagan, L.M. and J.G. Sclater, (1997) Digital Isochrons of the World's Ocean Floor. *J. Geophys. Res.*, 102, 3211–3214.

Natland, J.H. and Winterer, E.L., (2005), Fissure control on volcanic action in the Pacific. *GSA Special Paper*, 388, 687–710.

Nishimura, C.E. and Forsyth, D.W., (1989), The anisotropic structure of the upper mantle in the Pacific. *Geophys. J.*, 96, 203–229.

Nolet, G., Karato, S.-I. and Montelli, R., (2006), Plume fluxes from seismic tomography. *Earth Planet. Sci. Let.*, 248, 685–699.

Okubo, P.G., Benz, H.M. and Chouet, B.A., (1997), Imaging the crustal magma sources beneath Mauna Loa and Kilauea volcanoes, Hawaii. *Geology*, 25, 867–870.

Olson, P., (1990), Hot Spots, swells, and mantle plumes. in: "Magma Transport and Storage", M.P. Ryan (ed.), John Wiley, New York, 33–51.

Phipps Morgan J., Morgan, W.J. and Price, E., (1995), Hotspot melting generates both hotspot volcanism and a hotspot swell? *J. Geophys. Res.*, 100, 8045–8062.

Priestley, K. and Tilmann, F., (1999), Shear-wave structure of the lithosphere above the Hawaiian hot spot from two-station rayleigh wave phase velocity measurements. *Geophys. Res. Let.*, *26*, 1493–1496.

Raitt, R.W., (1956), Seismic-refraction studies of the Pacific Ocean Basin. Part 1: Crustal Thickness of the Central Equatorial Pacific. *Bull. Geol. Soc. Am.*, *67*, 1623–1640.

Rapp, R.H., Wang, Y.M. and Pavlis, N.K., (1991), The Ohio State 1991 Geopotential and Sea Surface Topography Harmonic Coefficient Models. *Dept. of Geodetic Science and Surveying, The Ohio State Univ., Columbus Ohio*, Rep. No, 410.

Renkin, M. and Sclater, J.G., (1988), Depth and age in the North Pacific. *J. Geophys. Res.*, *93*, 2919–2935.

Ribe, N.M. and Christensen, U.R., (1994), Three-dimensional modelling of plume-lithosphere interaction. *J. Geophys. Res.*, *99*, 669–682.

Ribe, N.M., (2004), Through thick and thin. *Nature*, *427*, 793–795.

Ritzwoller, M.H., Shapiro, N.M. and Zhong, S.-J., (2004), Cooling history of the Pacific lithosphere. *Earth Planet. Sci. Let.*, *226*, 69–84.

Robinson, E.M., (1988), The topographic and gravitational expression of density anomalies due to melt extraction in the uppermost oceanic mantle. *Earth Planet. Sci. Let.*, *90*, 221–228.

Ryall, A. and Bennett, D.L., (1968), Crustal Structure of Southern Hawaii Related to Volcanic Processes in the Upper Mantle. *J. Geophys. Res.*, *73*, 4561–4582.

Sato, H., Sacks, S. and Murase, T., (1989), The Use of Laboratory Velocity Data for Estimating Temperature and Partial Melt Fraction in the Low-Velocity Zone: Comparison With Heat Flow and Electrical Conductivity Studies. *J. Geophys. Res.*, *94*, 5689–5704.

Schutt, D.L. and Humphreys, E.D., (2004), *P* and *S* wave velocity and V_P/V_S in the wake of the Yellowstone Hot Spot. *J. Geophys. Res.*, *109*, B01305, doi:10.1029/2003JB002442.

Shor, G.G., (1960), Crustal Structure of the Hawaiian Ridge near Gardner Pinnacles. *Bull. Seism. Soc. Am.*, *50*, 563–573.

Sleep, N.H., (1990), Hotspots and mantle plumes: Some phenomenology. *J. Geophys. Res.*, *95*, 6715–6736.

Smith, M.L. and Dahlen, F.A., (1973), The azimuthal dependence of Love and Rayleigh wave propagation in a slightly anisotropic medium. *J. Geophys. Res.*, *78*, 3321–3333.

Stange, S. and Friederich, W., (1993), Surface wave dispersion and upper mantle structure beneath southern Germany from joint inversion of network recorded teleseismic events. *Geophys. Res. Let.*, *20*, 2375–2378.

Trampert, J. and Woodhouse, J.H., (1996), High-resolution global phase velocity distributions. *Geophys. Res. Let.*, *23*, 21–24.

van der Sluis, A. and van de Vorst, H.A., (1987), Numerical solution of largem sparse linear systems aris-

ing from tomographic problems. in: "Seismic Tomography", G. Nolet (ed), D. Reidel Publishing Company, Dordrecht, 49–83.

Vernon, F.L., Collins, J.A., Orcutt, J.A., Stephen, R.A., Peal, K., Wolfe, C.J., Hildebrand, J.A. and Spiess, F.N., (1998), Evaluation of Teleseismic Waveforms and Detection Thresholds From the OSN Pilot Experiment. *EOS Trans. AGU*, 79, F650.

von Herzen, R.P., Detrick, R.S., Crough, S.T., Epp, D. and Fehn, U., (1982), Thermal Origin of the Hawaiian Swell: Heat Flow Evidence and Thermal Models. *J. Geophys. Res.*, 87, 6711–6723.

von Herzen, R.P., Cordery, M.J., Detrick, R.S. and Fang, C., (1989), Heat Flow and the Thermal Origin of Hot Spot Swell: The Hawaiian Swell Revisited. *J. Geophys. Res.*, 94, 13,783–13,799.

Watts, A.B., (1976), Gravity and Bathymetry in the Central Pacific Ocean. *J. Geophys. Res.*, 81, 1533–1553.

Watts, A.B. ten Brink, U.S., Buhl, P. and Brocher, T.M., (1985), A multichannel seismic study of lithospheric flexure across the Hawaiian–Emperor seamount chain. *Nature*, 315, 105–111.

Webb, S.C. (1998), Broadband Seismology and Noise Under the Ocean, *Rev. Geophys.*, 36(1), 105–142.

Willoughby, D.F., Orcutt, J.A. and Horwitt, D., (1993), A microprocessor–based ocean–bottom seismometer. *Bull. Seismol. Soc. Am.*, 83, 190–217.

Wilson, J.T., (1963), A possible origin of the Hawaiian Islands. *Can. J. Phys.*, 41, 863–868.

Wolfe, C.J., Bjarnason, I.T., vanDecar, J.C. and Solomon, S.C., (1997), Seismic structure of the Iceland mantle plume. *Nature*, 385, 245–247.

Wolfe, C.J., Solomon, S.C., Silver, P.G., vanDecar, J.C. and Russo, R.M. (2002), Inversion of body–wave delay times for mantle structure beneath the Hawaiian Islands; results from the PELENET experiment. *Earth Planet. Science Let.*, 198, 129–145.

Woods, M.T., Leveque, J.–J., Okal, E.A. and Cara, M., (1991), Two–station measurements of Rayleigh wave group velocity along the Hawaiian Swell. *Geophys. Res. Let.*, 18, 105–108.

Woods, M.T. and Okal, E.A., (1996), Rayleigh–wave dispersion along the Hawaiian Swell: a test of lithospheric thinning by thermal rejuvenation at a hotspot. *Geophys. J. Int.*, 125, 325–339.